Accepted in “Journal of Manufacturing Processes” on 12th October 2024

A novel approach for the removal of oxide film to achieve seamless joining during hot-compression bonding

Yong Zhao [1], Bin Xu [2], Saurav Goel [3,4], Haojie Xu [1], Kuo Li [2], Danka Labus Zlatanovic [5], Mingyue Sun [2], Jiang Guo[1,*], Renke Kang[1] and Dianzhong Li [2]

[1] State Key Laboratory of High-performance Precision Manufacturing, Dalian University of Technology, Dalian, 116024, China
[2] Shenyang National Laboratory for Materials Science, Institute of Metal Research, Chinese Academy of Sciences, Shenyang, 110016, China
[3] China Beacons of Excellence Research and Innovation Institute (CBI), University of Nottingham Ningbo China (UNNC), Ningbo, 315101, China
[4] Department of Mechanical Engineering, University of Petroleum and Energy Studies, Dehradun, 248007, India
[5] Department of Production Technology, Technische Universität Ilmenau, Ilmenau, 98693, Germany

E-mail: guojiang@dlut.edu.cn

Abstract

The oxide film on the substrate surfaces can severely hinder the bonding quality during hot-compression bonding (HCB). To address the above issue, this investigation proposes a novel approach to enhance bonding quality by removing surface oxide film and encapsulating the interface to be bonded in sequence under vacuum. The principle of the approach was clarified, and an experiment platform used for implementing the approach was designed and developed. By considering 316H stainless steel as a testbed, the key parameter for laser ablation of the oxide films before HCB was determined. The HCB comparative experiments of substrates with or without treatment by the approach were carried out and the effectiveness of the approach was assessed by comparing the quality of bonding joints through interface morphologies and tensile properties. Results showed that a nearly seamless bond without thermal holding was achieved after adopting this approach. Further, it also showed improvement in the tensile properties both in elongation and the ultimate tensile strength (UTS). For instance, when using the proposed approach, the average UTS of 316H stainless steel joints improved from 371.17 MPa to 430.25 MPa whereas the average elongation increased from 26.41% to 64.04%. Although this investigation was directed to 316H stainless steel, the suggested approach can be applied to a wide range of other engineering materials to improve the joining quality.

Keywords： Vacuum; Laser treatment; Oxide film; Hot-compression bonding; Seamless joining

1. Introduction

Additive forging technology is widely used to manufacture heavy forgings with the main objective of achieving seamless bonding. Additive forging uses high-quality casting slabs as substrates and the process entails manufacturing processes involving surface treatment, substrate stacking, vacuum electron beam welding and hot-compression bonding (HCB) [1]. During this process, the HCB process is a critical step for achieving seamless bonding. However, for metals that are susceptible to atmospheric oxidation, the compact oxide film on the metallic surface can severely hinder the bonding quality and the residual oxide film or oxide particles further reduce the effective bonding area of the interface paving the way for the early mechanical failure [2]. Therefore, it is essential to address the hindrance effect caused by the interfacial oxide film during the HCB process. Generally, three approaches for HCB or similar other manufacturing processes can be taken to address this issue recently.

The first category concerns breaking the oxide film using external high pressure. Zlatanovic et al. [3] characterized the microscopic features of the weld faying interface in the solid state joining of aluminum alloys, it was demonstrated that the intact oxide film was converted to oxide fragments under the impact of the introduced force. The fragmentation of oxide film can promote diffusion, however, the residual oxides and nano-pits on the interface can act as the initiating source of interfacial delamination. Zhao et al. [4] proposed a novel ultrasonic-assisted approach to joining 6063 aluminum alloys. In this approach, a Zn interlayer was added between the substrates so that the surface oxide film diffuses to the Zn layer at 360℃ and breaks instantly into small fragments during ultrasonic vibration loading. As a result, the homogeneous joints with the eutectic phase with high strength containing oxide fragments were fabricated. Similarly, Xu et al. [5] reported an investigation concerning ultrasound-assisted breaking of the oxide film on the surface to be bonded to promote the bonding quality. In addition, Zuruzi et al. [6] proposed a technique for addressing this issue during the diffusion joining of 6061 aluminum alloys. The technique induced relative motion at the interface to break the oxide film when the diffusion bonding was carried out. The results showed that the ultimate tensile strength (UTS) and interface bonding rate of the bonding joint were greatly improved through this technique. Thus, the first category of approaches shows an effective outcome to mitigate the hindering effect caused by the oxide film. However, the broken oxide film entrapped in the interface inevitably affects the mechanical properties of the bonding joints.

The second category concerns increasing the duration of holding the high temperature after rupturing the oxide film. For many metallic materials, the oxide film can dissolve into the matrix under specific conditions [7], which opens up the possibility of addressing the hindering effect caused by the surface oxide film. Xie et al. [8] proposed an approach to diffuse the oxide film at high temperatures after breaking the interfacial oxide film. Their results showed that the tensile properties of 316 stainless steel bonded joints reached the same levels as the base materials after holding it at 1200℃ for more than 18 h. Zuo et al. [9]

prepared carbon nanotube reinforced aluminum-4Cu-1Mg bonded joints by HCB with 485℃ under 50% deformations and then held them for 2 h to promote the bonding. The results showed a bonding joint with a tensile strength of 384 MPa was obtained, the deformation can facilitate interfacial bonding as the oxide film was broken effectively. In addition, the holding treatment promoted the dissolution of interfacial oxide resulting in achieving seamless bonding. This type of approach minimized the effect of the oxide film on the interface bonding; however, it is only effective for metals that are susceptible to dissolved oxygen. In addition, it relies on holding temperature, holding time and deformation, the oxygen remains entrapped in the matrix. This approach has limitations, for example, for large substrates, it is difficult to break the oxide film completely. In contrast, removing the oxide film before HCB can exclude oxygen from the bonding joints and reduce the reliance on the HCB parameters.

The third category of approaches concerns the removal of surface oxides from the substrates under the atmospheric environment prior to the HCB process. For example, Liu [10] proposed a pretreated strategy to inhibit the hindering effects posed by the oxide film. In this pretreatment electrolytic corrosion was used to remove the oxide film under the atmospheric environment. It was shown that the oxides on the interface of the bonded joints hot-compressed by the pretreated substrates were significantly reduced. The tensile and durability properties of the bonding joints were substantially improved. In addition to these three approaches, there are many other methods for removing the oxide films under atmospheric conditions, such as mechanical grinding [11] and laser cleaning [12]. However, as these methods are carried out in environmental conditions, the susceptibility for the formation of oxides exposes the fresh metal surface to redevelop a new oxide layer by reacting with the environmental oxygen. Although the third category discussed above mitigates the issue of surface oxides, the freshly exposed metal can largely undergo secondary oxidation which limits seamless joining.

As shown in Fig 1, the principles and problems of the three types of approaches used to mitigate the interfacial bonding hindrance caused by the oxide film were summarized. It may be seen that some limitations persist. To address the issue of oxide films adversely influencing the quality of joining as well as avoid the limitations of existing approaches, a new approach is needed. A valid hypothesis was to remove the oxide film under vacuum before HCB and inhibit the secondary oxidation after removing the oxide film allowing the freshly exposed metal to join seamlessly. However, it is a challenging proposition. Especially, few feasible approaches can prevent secondary oxidation before HCB.

Laser cleaning in a vacuum seems to be a scalable and feasible technique for removing the oxide films. Pulsed laser irradiates a high-energy density beam onto the surface to be treated in a short period of time to perform the function. It possesses many advantages, such as high efficiency; small heat affected zones due to fast heating and cooling rates; high processing accuracy; available for different materials and shapes of substrates; low contaminants introduced and easy integration with automation carriers. The above advantages make it widely used to remove oxide film in the atmospheric environment [13]. However, laser

cleaning in atmospheric conditions can lead to secondary oxidation [14]. While they demonstrated good use of laser cleaning under atmospheric conditions, they did not consider the issue of secondary oxidation while exposing the air to fresh metal. Consequently, while the oxide film removal under atmospheric conditions through laser was considered effective, it is also clear that isolating the oxygen reaction with metal is essential.

To remedy the hindrance effect of interfacial bonding caused by the oxide film completely and thereby achieve the objective of improving the bonding quality, this work proposed a novel approach, namely, removing the oxide film, assembling the substrate to be joined and welding the contact edges of the assembled substrate in sequence under vacuum, keeping the surface to be joined free from the original oxide film and secondary oxidation completely.

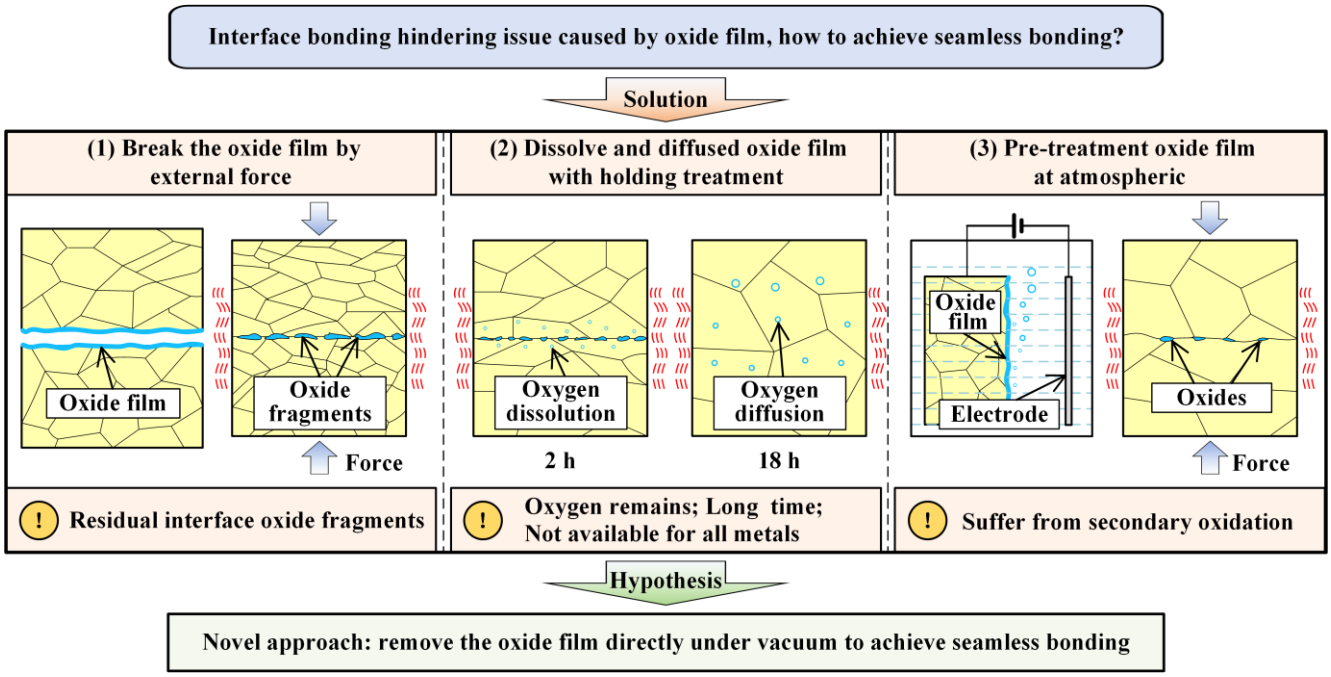

Fig. 1. Principle of three strategies to remedy the oxide films discussed in the literature

2. Principle of the approach

The underlying principle of the proposed approach is shown in Fig. 2. In vacuum conditions, the laser was used to remove the oxide film on the substrate surface. Subsequently, the substrates were assembled and then welded by the vacuum electron beam system, maintaining the bonding surfaces in an oxygen-free environment continually.

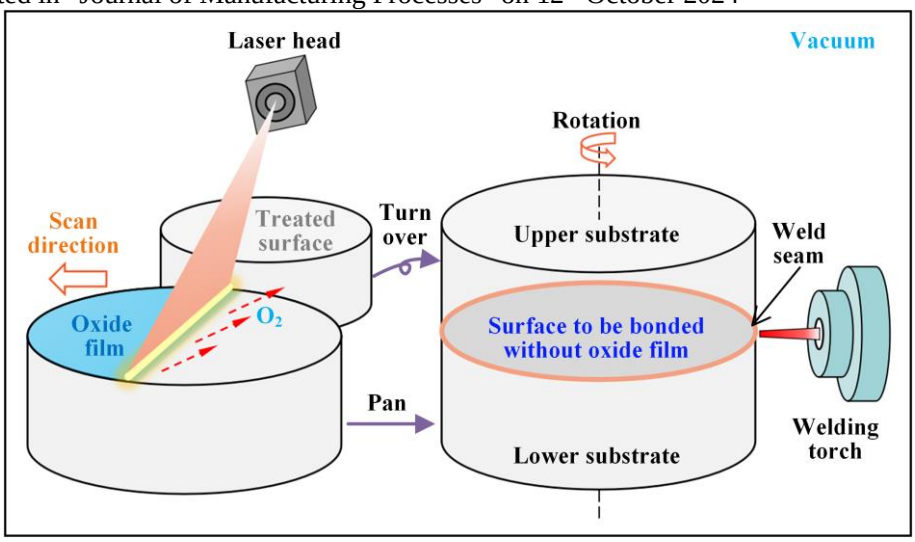

Fig. 2. Schematic diagram of the approach to enhance the bonding quality by removing the surface oxide film

The platform developed to execute this approach is shown in Fig. 3. It consists of three parts namely, the robotic arm, the laser and the electron beam welding system. The vacuum cavity of the electron beam welding system can produce a vacuum of around 5×10^{-2} Pa. The mobile platform was used to adjust the position between the robotic arm and the welding torch. A robotic arm with gripper jaws was installed on the mobile platform to transit and stack the substrates. The controller of the robotic arm system was placed out of the vacuum cavity and the power supply and signals for the robotic arm and controller were connected via a specially designed vacuum plug. The vacuum plug ensured that the vacuum cavity was sealed. The laser head was installed on the inner wall of the vacuum cavity and the controller was placed out of the vacuum cavity. The connection was similar to the robotic arm system. The difference is that the optical fiber needs to pass through the vacuum plug and the gap needs to be sealed. The electron beam welding system was used to weld the stacked substrates. The rotation of the rotating platform enables the entire welding of the stacked substrates.

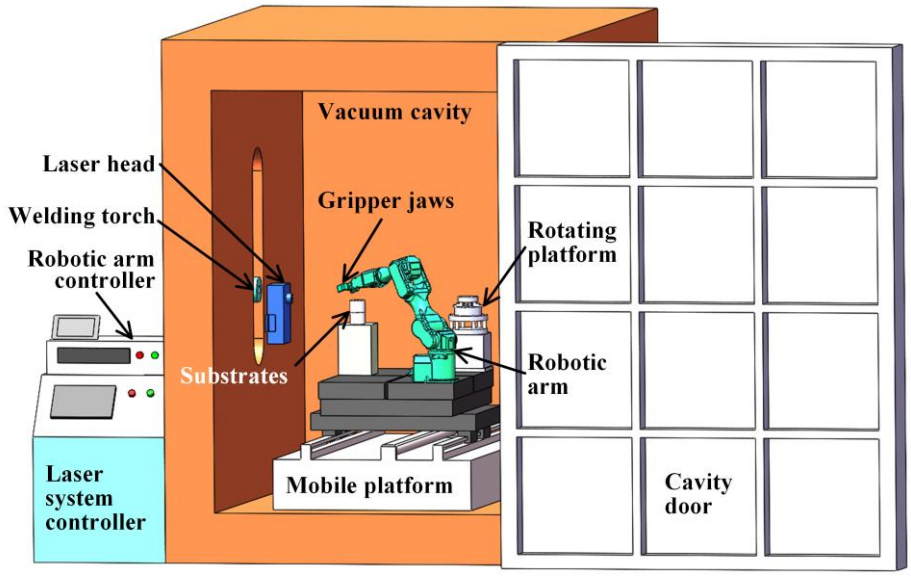

Fig. 3. Schematic diagram of the platform developed for laser-removal of oxide film under vacuum.

The critical steps followed to remove the oxide films under vacuum are shown in Fig. 4. Both substrates were treated, and the robotic arm was held in the initial position, the vacuum cavity forms a sealed space after the cavity door is closed and the gas in the vacuum cavity was pumped out to form a stable vacuum atmosphere. The critical steps of the approach involved in the removal of the oxide film under vacuum prior to the HCB process were (a) The robotic arm grips the upper substrate, moves and rotates the substrate, placing the surface to be treated towards the laser head and stops at the focal length of the laser. (b) Setting of the laser parameters while irradiating it on the substrate surface (c) The robotic arm rotates the upper substrate placing the treated surface face upwards. (d) The robotic arm grips the lower substrate, moves and rotates the substrate, places the surface to be treated towards the laser head and stops at the focal length of the laser. (e) Laser beam irradiates the substrate surface to be treated until the entire surface of the lower substrate was scanned. (f) The robotic arm transfers to the lower substrate making the treated surface face downwards and contact with the treated surface of the upper substrate. (g) Weld the contact edges of the upper and lower substrates to keep the interface bonded in a vacuum state consistent with the vacuum cavity. The welded sample was removed from the vacuum cavity, heated and forged in atmospheric conditions.

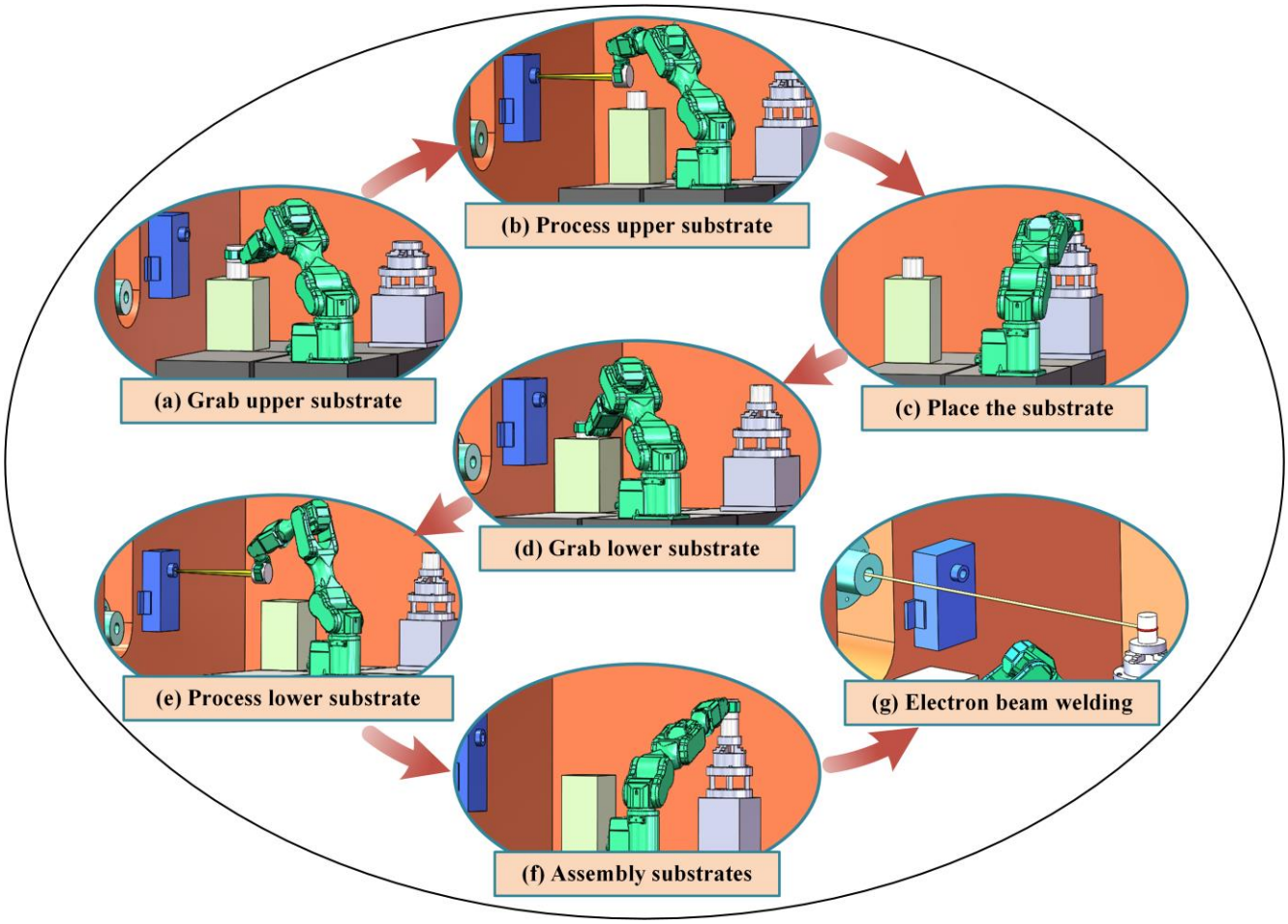

Fig. 4. Steps followed to remove the oxide films under vacuum

3. Materials and experimental details

3.1 Materials and substrates pretreatment

316H stainless steel was selected as the preferred material due to its application in heavy components and its low oxidation resistance. 316H stainless steel can form a dense surface oxide film quickly on exposure to the atmosphere. The chemical composition of the 316H stainless steel used in this work is shown in Table 1.

Table 1 Chemical composition of the 316H stainless steel (wt. %).

Elements	C	Mn	Si	Cr	Ni	P	S	Mo	Fe
Content	0.07	1.70	0.35	17.69	11.59	0.04	0.02	2.91	Bal.

Four pieces of 316H stainless steel substrates with dimensions of Ø100 × 45 mm were prepared. The surfaces were ground and cleaned to remove any defects and contaminants. After pretreatment, the substrates were left under atmospheric conditions for 36 h to form a dense oxide film. Two pieces of pretreated original substrates were used for removal of the oxide film under vacuum. Another two substrates were used as control samples without removing the oxide films. To characterize the surface oxides, a sample with dimensions of 10×10×5 mm was derived from the 316H stainless steel substrates, the surface to be measured was ground until it was flat, then the sample was cleaned in alcohol solution for 5 minutes by ultrasonic to remove contaminants, keeping the surface to be measured fresh. The sample was blown dry and placed in the sample box to stay for 36h waiting for the test. Finally, the sample was glued to a non-conductive glass sheet for testing. The chemical compositions of the ground surfaces were analyzed using X-ray Photoelectron Spectroscopy (XPS). The radiation source of the XPS (Axis Supra+, Japan) was Kα rays of the monochromatic Al with an energy of 1486.6 eV. The survey spectra were recorded using 1.0 eV step sizes with a pass energy of 160 eV. Elemental spectra were collected using 0.1 eV step sizes with a pass energy of 40 eV. The contaminated carbon C 1s signal at 284.8 eV was used to calibrate binding energy. The XPS curve fitting was carried out with the Avantage software.

3.2 Process of laser surface treatment

The experiment of laser removal of the oxide film under vacuum was carried out by using the setup shown in Fig. 5. Two pretreated substrates were placed at the initial position. The experiments were carried out by following the steps described in Section 2. The experiment was monitored by a camera fitted inside the vacuum cavity. The vacuum pressure during laser ablation of the oxide layer was maintained at 5×10^{-2} Pa. COMSOL software Version 6.1 was used to model and estimate the optimal laser energy. In the simulations, the laser frequency was kept constant at 300 kHz and the laser energy was adjusted by varying the average laser power of 60 W, 120 W and 180 W corresponding to 0.2 mJ, 0.4 mJ and 0.6 mJ, respectively. The average laser power was converted to peak laser power used for simulation. The average laser power

used for the experiment was determined by the optimal laser energy calculated from the simulations. The main laser parameters for laser-removal of the oxide films used for the experiment are shown in Table 2. The depth of the weld seam was 10 mm which is much smaller than the diameter of the surface to be bonded. Thus, the weld did not affect the interface to be bonded.

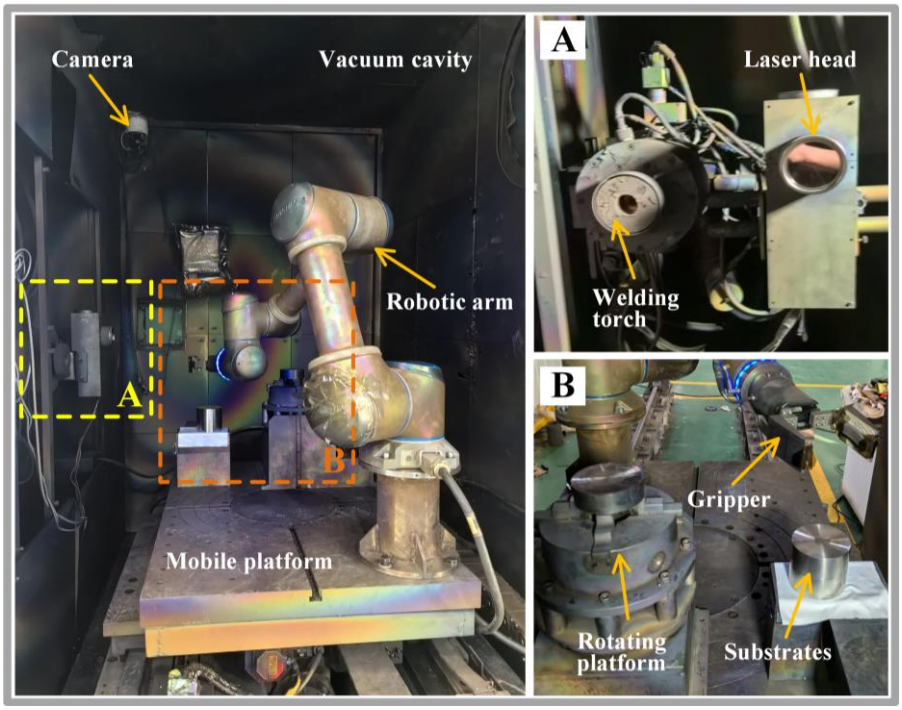

Fig. 5. Experiment setup for laser-removing oxide film under vacuum.

Table 2 Parameters for laser-removing oxide film used for the experiment.

Parameters	Value
Wavelength λ/(nm)	1064
Pulse width *n*/(ns)	100
Average laser power *P*/(W)	120
Frequency *f*/(kHz)	300
Scanning speed *v*/(mm/s)	8100
Spot diameter D/(μm)	62.6

3.3 Process of hot-compression bonding

Fig. 6(a) shows the summary of experimental steps followed to perform the HCB. 1# welded sample was welded by substrates treated by the proposed method (by removal of the oxide film from the mating surfaces). The 2# welded sample was welded by substrates without treatment, to be benchmarked as the control group, namely with the native oxide film. The 1# and 2# welded samples were both welded under the same vacuum of 5×10^{-2} Pa. Thus, the vacuum conditions of the interface during the bonding process were kept the same. The high-temperature oxidation behavior of the interfaces to be bonded was effectively suppressed. The sole difference between the two sets of experiments was whether the native oxide film on the surface to be bonded was removed under vacuum. To ensure the interfaces to be bonded of the welded

samples remained in vacuum, the welded seams were detected for vacuum breakage by using the dye penetrant inspection materials. Afterwards, the welded samples were heated and forged. Two sets of welded samples were heated to 1050°C and then held for 2 h in the same heating furnace, making the temperature of the substrate homogeneously, in particular, ensuring the inner temperature of the substrate reached 1050 °C as well. At such high temperatures and such long holding time, the introduced residual stresses can be sufficiently released, thus, the effect of residual stresses was negligible. Then the heated samples were simultaneously forged by the same forging machine. The deformation strain, temperature and strain rate of the two sets of welded samples were found consistent. The temperature of the HCB was 1050°C and the deformation strain was 20%. During the HCB process, the insulation cotton was used to isolate the heat exchange between the compressed samples and the squeezed head. The 1# bonding joint was hot-compressed by 1# welded sample and the 2# bonding joint was hot-compressed by 2# welded sample. The HCB experiment was repeated three times to ensure stability and reproducibility of the results.

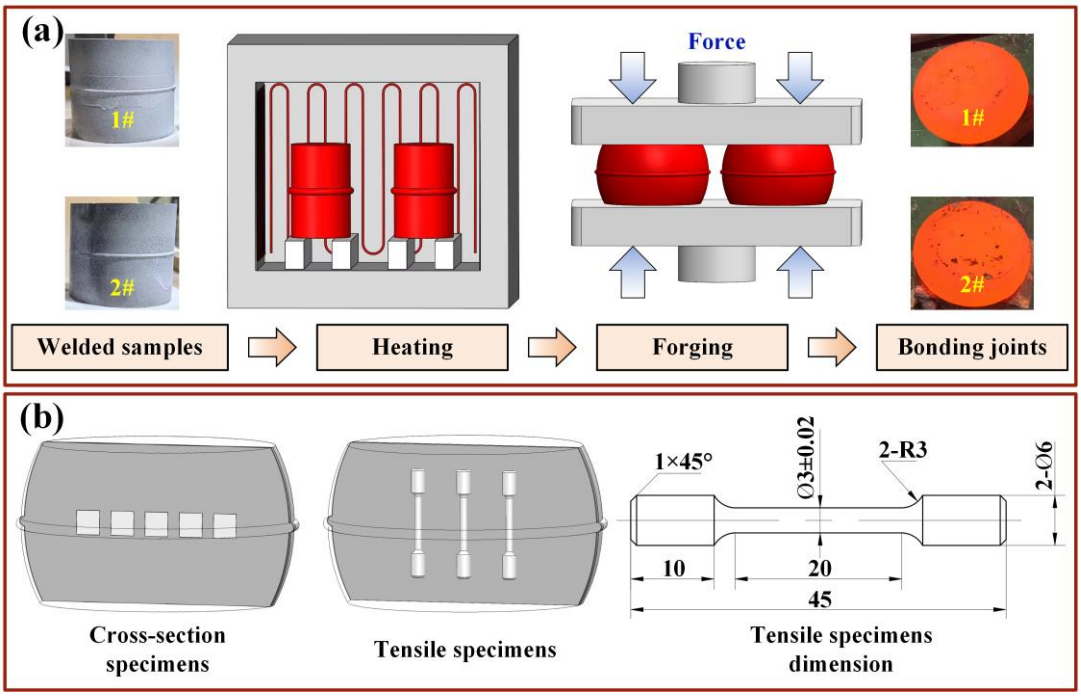

Fig. 6. Schematic diagram of (a) the HCB process, (b) the test specimen preparation process.

3.4 Preparation and characterization of test specimens

Bonding joints were cut along the center in a direction perpendicular to the bonding interface. The cross-section and tensile specimens were prepared as per the standard test protocols (see Fig. 6(b)). The cross-section and tensile specimens were derived near to the center of the bonding joints and the sampling locations of the 1# and 2# bonding joints were kept consistent. The cross-section specimens were ground and polished until a scratch-free surface was obtained. Finally, the specimens were electro-etched with 10% $H_2C_2O_4$ (vol%) solution at 12V and 2A. Zeiss metallurgical microscope (Axio Scope 5, Germany) was used to observe the microscopic morphology of the interface. Scanning electron microscopy (SEM) (SU5000,

Japan) with energy dispersive spectroscopy (EDS) was used to observe the morphology and detect elements. The dimensions of the tensile specimens are shown in Fig. 6(b), the tensile specimen surface was ground to remove scratches. The tensile tests were performed at room temperature at a strain rate of 1 mm/min by using the tensile testing machine (Instron-5982, USA). Three sets of parallel tensile specimens were derived from 1# and 2# bonding joints. SEM was used to observe the fracture morphology of tensile specimens and EDS was used to analyze elements.

4. Results and discussions

4.1 The key parameter for laser-removal of the oxide film

4.1.1 Surface oxide film characterization

The oxide film was comprehensively characterized to establish the most robust laser ablation parameters for removal of the oxide film. Fig. 7 shows the XPS spectra of the substrate surface after grinding under atmospheric conditions. Fig. 7(a) shows the result of the survey scans, the main peaks were Fe 2p, Cr 2p, O 1s and C 1s. The results were calibrated by the C 1s signal at 284.8 eV. It can be inferred from the survey scans that the native oxide film on the substrate surface was the oxide of Fe and Cr. Fig. 7(b) shows the high-resolution spectra of O 1s, revealing three types of features. The first was metal oxides with binding energies 532.0 eV, 529.1 eV and 529.7 eV corresponding to Fe_2O_3, Fe_3O_4 and Cr_2O_3, respectively [15-17]; The binding energy at 530.8 eV corresponds to the metal hydroxide $Cr(OH)_3$ [18]. The binding energy 532.8 eV corresponds to adsorbed water [19], the presence of water and hydroxides is related to the moisture in the atmosphere. To further verify the type of oxide film, split peaks were fitted to the high-resolution spectra of Fe 2p and Cr 2p. The fitting results of the high-resolution XPS spectra for Fe 2p presented in Fig. 7(c) suggest that the binding energy of Fe $2p^{3/2}$ and Fe $2p^{1/2}$ were 709.8 eV and 723.6 eV, respectively, which proves the presence of Fe_2O_3 [20]. Additional satellite peaks were also fitted at binding energies of 719.2 eV and 732.8 eV [21], which are characteristic of Fe_2O_3. The peaks at 711.0 eV and 724.6 eV belong to Fe^{3+} $2p^{3/2}$ and Fe^{3+} $2p^{1/2}$, respectively, while the peaks at 709.2 eV and 722.3 eV correspond to Fe^{2+} $2p^{3/2}$ and Fe^{2+} $2p^{1/2}$ [22] and the presence of Fe^{3+} and Fe^{2+} indicated Fe_3O_4 in the oxide film. The above peaks correspond to the oxidation state of Fe. However, a weaker peak was also fitted at a binding energy of 706.3 eV (Fe $2p^{3/2}$), this peak corresponds to the metallic Fe [23]. Fig. 7(d) exhibits the fitting results of Cr 2p, the high peaks of binding energy at 576.2 eV (Cr $2p^{3/2}$) and 585.8 eV (Cr $2p^{1/2}$) indicated that a large amount of Cr^{3+} exists as Cr_2O_3 [24]. In addition, Cr $2p^{3/2}$ and Cr $2p^{1/2}$ showed weak peaks of binding energy at 577.1 eV and 586.8 eV, corresponding to $Cr(OH)_3$ [25]. The binding energy at 573.5 (Cr $2p^{3/2}$) in the high-resolution spectra of Cr 2p corresponds to metallic Cr [23]. As can be seen from the results of the survey scans and high-resolution spectra, the native oxide film of the substrate was a mixed oxide of Fe and Cr, the metal oxides were mainly Fe_2O_3, Fe_3O_4 and Cr_2O_3.

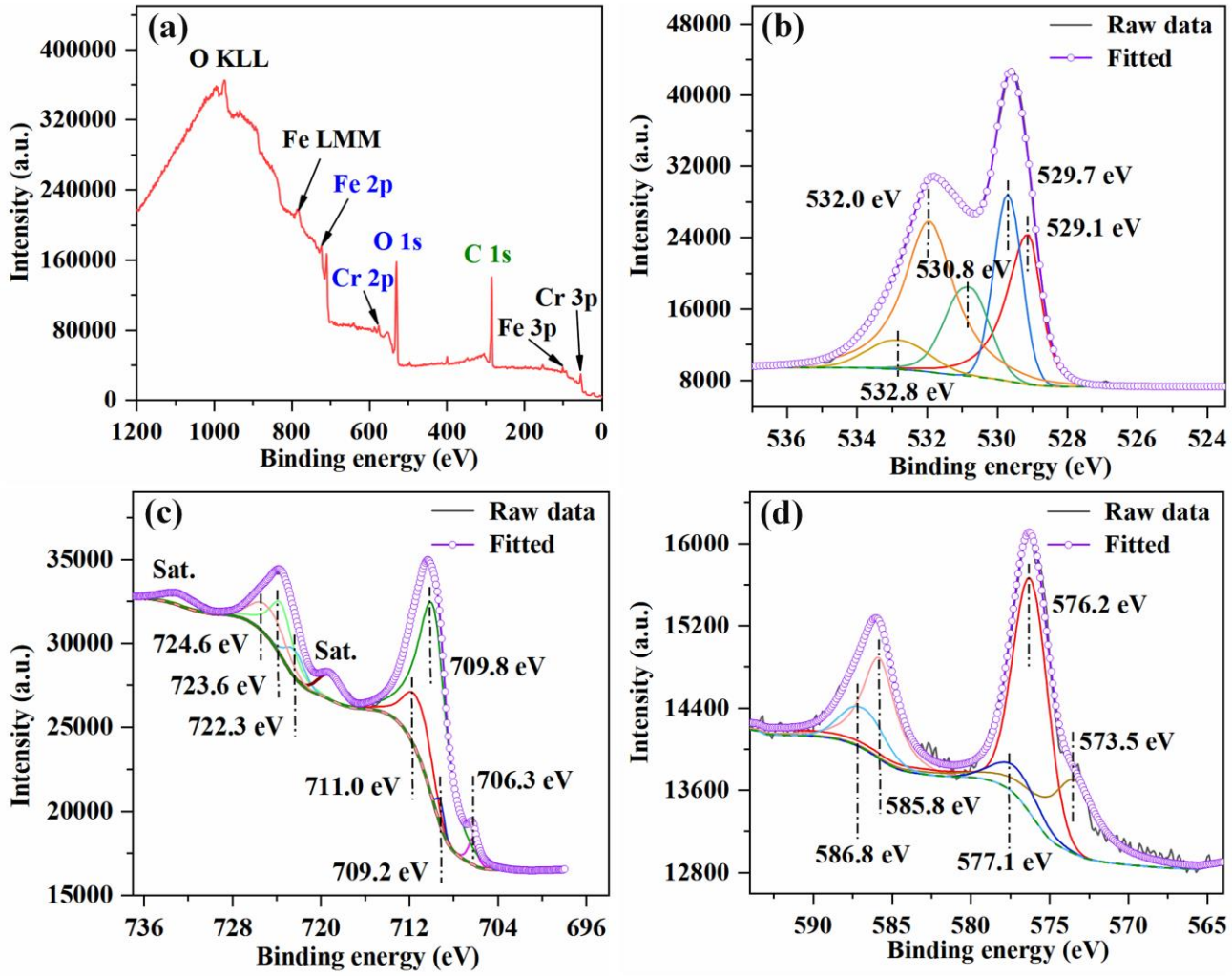

Fig. 7. XPS spectra of the substrate with native oxide film. (a) survey scans, (b) O 1s, (c) Fe 2p, (d) Cr 2p.

4.1.2 Simulation output of the optimal laser energy

According to the XPS results, the oxide film contained Fe_2O_3, Fe_3O_4 and Cr_2O_3, the metal oxide Fe_3O_4 tends to decompose at 1811 K to Fe_2O_3. Based on the literature, it is known that the boiling points of metal oxides Cr_2O_3 and Fe_2O_3 are 4273 K and 3687 K, respectively [26, 27]. The highest boiling point of substances in the oxide film is Cr_2O_3, with a boiling point of 4273 K. Therefore, the removal of the oxide film in entirety will require the laser to generate a temperature in excess of 4273 K. Laser energy is the key parameter that affects the irradiation temperature. To screen the available laser parameter, the temperatures generated for different laser energies were simulated. The substrate was set as 316H stainless steel with a triangular mesh while the oxide film was set as Cr_2O_3 with a quadrilateral mesh. The laser has a Gaussian profile, the distribution of energy density in the laser spot has Gaussian form [28]:

$$E(r) = E_0 \exp(\frac{-2r^2}{\omega_0^2}) \quad (1)$$

where E_0 is the maximum energy and ω_0 is the radius of the laser spot.

The simulation input variables were the laser energy of 0.2, 0.4 and 0.6 mJ, however, the laser energy

density per pulse is important [29, 30]. So, the energy density of the laser spot was calculated to help understand the process of laser removal of oxide film. The laser energy densities were 6.51 J/cm^2, 13.03 J/cm^2 and 19.54 J/cm^2, corresponding to a laser power of 0.2, 0.4 and 0.6 mJ. Fig. 8 shows the temperature field distribution and temperature variation curves for different laser energies, the blue dashed lines in the figure indicate the required temperature for oxide film vaporization removal, namely 4273 K. As shown in Fig. 8(a), the maximum temperature was below 4273 K when the laser energy was 0.2 mJ. Fig. 8(b) shows the distribution of temperature field at 2.34×10^{-5} s, the maximum temperature reached 4134 K. When the laser energy was 0.4 mJ, the maximum temperature increased and exceeded 4273 K, which can vaporize the oxide film. The increase in temperature is mainly due to the increased laser energy density. In addition, the temperature distribution within the laser spot is consistent with a Gaussian energy density distribution form. The high-temperature area spot was large, the maximum temperature can reach 4335 K at the same time, as shown in Fig. 8(c) and (d). The laser energy has fulfilled the requirement of removing the oxide film and the high efficiency of oxide film removal can be realized. As the laser energy reaches 0.6 mJ, the maximum temperature further increased, the range of the high-temperature region further expanded, the maximum temperature reached 4449 K at time of 2.34×10^{-5} s, as shown in Fig. 8(e) and (f).

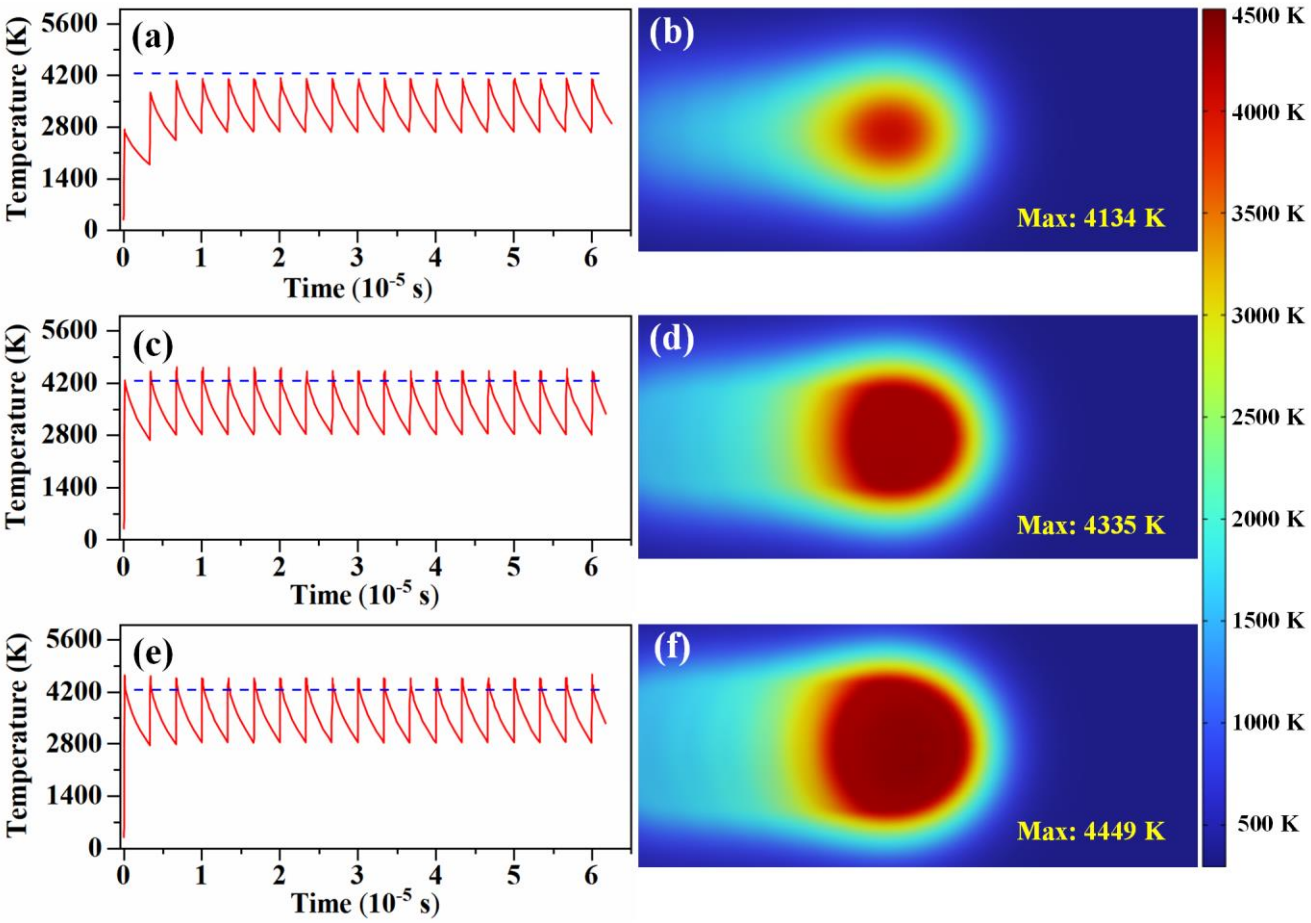

Fig. 8. Temperature variation curves with time and temperature field distribution for different laser energies. (a) (b) 0.2 mJ, (c) (d) 0.4 mJ, (e) (f) 0.6 mJ.

In summary, the maximum temperature and the range of high-temperature regions increases with the increasing of the laser energy, considering the maximum temperature and the temperature field distribution, the laser energy of 0.4 mJ was considered as the suitable parameter to remove oxide film under vacuum. The correctness of the simulation results can be indirectly proved by the interface bonding quality.

4.1.3 Surface morphologies of the substrate with or without laser treatment

Adequate characterization facilitates the realization of a better understanding of the object [31]. Fig. 9 shows the surface morphologies of the substrate with or without laser treatment, the original surface of the substrate consists of sharp peaks and valleys, the scratches are extremely noticeable. In contrast, the surface of the substrate was smoothed after laser removal of the oxide film under vacuum, the sharp peaks blunted. Meanwhile, some craters produced by the laser were observed.

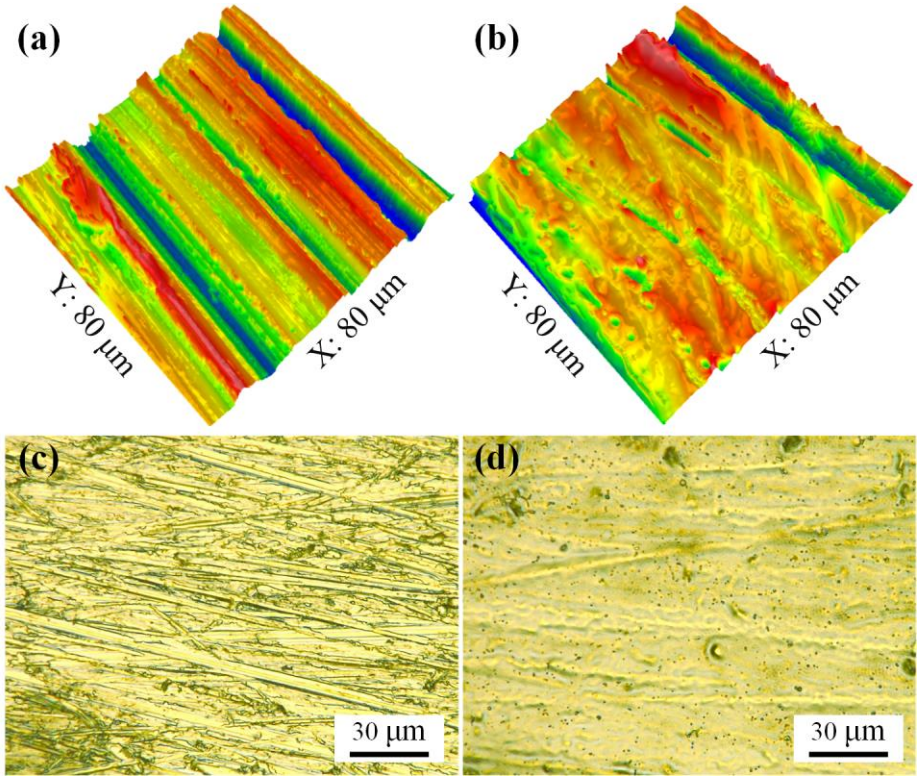

Fig. 9. Surface morphologies of the substrate. (a) 3D morphology of original surface (b) 3D morphology after laser treatment, (c) optical morphology of original surface, (d) optical morphology after laser treatment.

The process of laser removal of oxide films was complex, existing research shows that laser removal of oxide films was mainly influenced by thermal or force effects. Under the role of thermal effect, the oxide film is rapidly heated up and vaporized to remove, which mainly occurs in the oxide film that is tightly combined with the substrate [32]. As for the force effect, laser-induced stress waves lead to oxide stripping, which mainly occurs in oxide films that are not tightly bonded to the substrate, such as the oxide film produced after hot rolling [33]. The surface morphologies of the substrates produced by the two types of mechanisms are different. The surface of the substrate is blunted after being subjected to the thermal mechanism. In contrast,

the surface of the substrate after being subjected to the force mechanism can present cracks or other sharp features. The surface of the substrate after laser removal of the oxide film is blunted compared to the surface of the original substrate, which proved that the substrate surface was subjected to thermal effects. From the surface morphology after the laser removal of the oxide film and the simulation results in Section 4.1.2, it is inferred that the oxide film undergoes the process of heating and vaporization during the laser treatment. Pulsed lasers release high energy in a very short period and cool down immediately, from the surface morphologies, it can be recognized that the oxide film was removed with minimal or negligible impact on the substrate surface.

4.2 Interface bonding quality

The interface bonding quality of the joints was the most significant index to assess the effectiveness of the proposed approach. Interface bonding quality was characterized by cross-section morphologies, interface elements distribution and tensile properties. The following compared the interface bonding quality of 1# and 2# bonding joints.

4.2.1 Cross-section morphologies

Fig. 10 shows the cross-section morphology of the 1# bonding joint (treated with the proposed approach). The yellow arrows indicate the location of interfaces. These images confirmed seamless bonding. It proved that a better bonding with a high interfacial bonding ratio was achieved after removing the oxide film on the surfaces to be bonded of the substrates by the laser under vacuum. During the HCB process, recrystallization occurred at the interface and fine grains become distributed along the interface. Some of the recrystallized grains crossed the interface, as shown in the red circle in the enlarged images and the recrystallized grains that crossed the interface were highlighted in blue. The oxide film that acted as a barrier to the interfacial bonding got removed. Subsequently, the contact of fresh metal yielded stronger metallic bonding through an improved diffusion and migration of interfacial grain boundaries. This finding is in alignment with the previous reports [34].

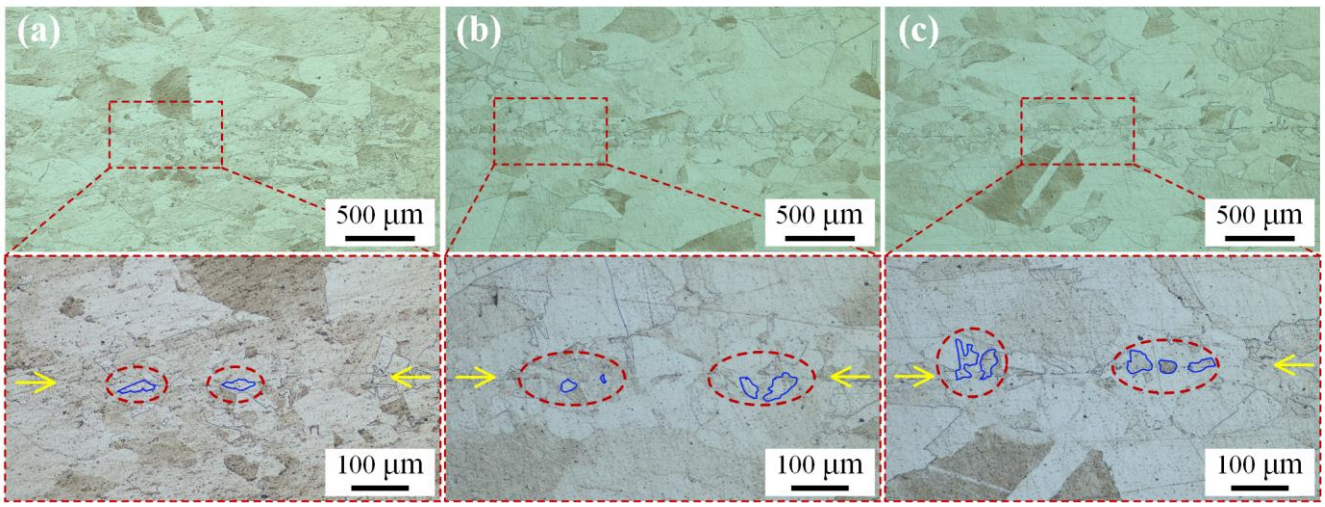

Fig. 10. Cross-section morphologies of the 1# bonding joint. (a), (b), (c) are from different specimens.

The cross-section morphology of the 2# bonding joint (without treatment) was different from the cross-section morphology of the 1# bonding joint. As shown in Fig. 11, the interface of the 2# bonding joint was visible and appears as a black line almost across the entire field of view, reflecting an extremely low ratio of interfacial bonding. In addition, there were also fine recrystallized grains distributed on both sides of the interface, as indicated by the blue arrows. Most recrystallized grains were blocked on both sides of the interface. The above phenomenon was caused by the interfacial oxides that hindered the migration of grains. However, small regions in the interfaces achieved good bonding with a few recrystallized grains crossing the interface which were marked with a red circle. This could be ascribed to the breakage of the oxide film at the interface under deformation during the HCB process, which results in part of the metal achieving direct contact. However, this bonding relies heavily on deformation and the remaining oxide film still acts as a barrier.

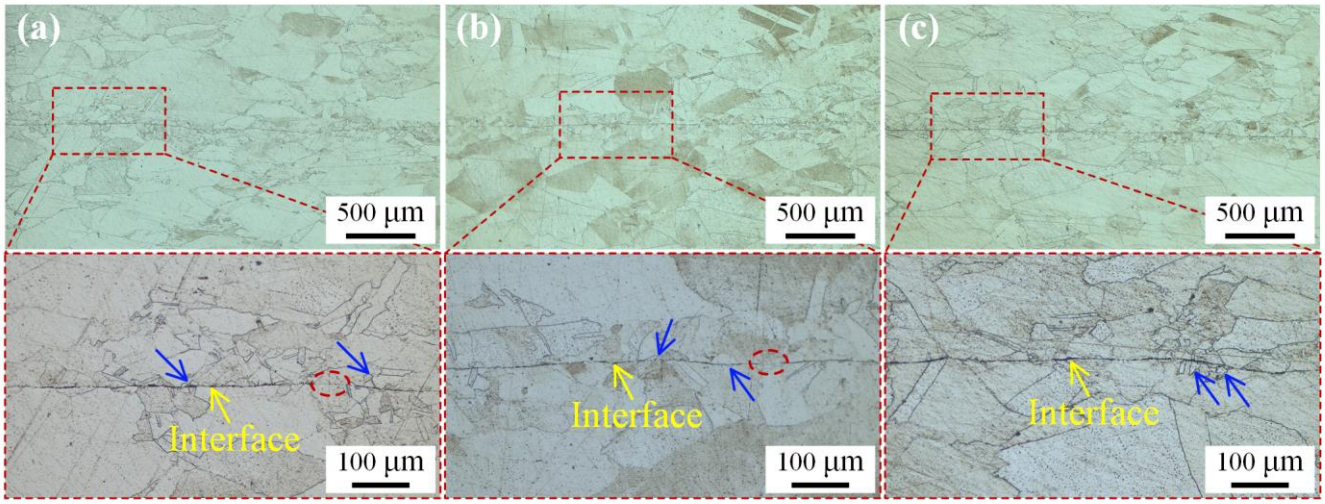

Fig. 11. Cross-section morphologies of the 2# bonding joint. (a), (b), (c) are from different specimens.

Fig. 12 shows the results of the repeated experiments on the cross-section morphologies, three repeated HCB experiments were carried out after using the proposed approach. The cross-section morphologies of the center positions of the obtained bonding joints are shown in Fig. 12 (a) (b) and (c). The cross-section morphologies showed favorable consistency, the interface almost achieved seamless bonding, the bonding characteristics were generally consistent with those shown in Fig. 10. Fig. 12 (d) (e) and (f) are the cross-section morphologies of the bonding joints obtained from three repeated control experiments. The interfaces were all visible, the results were aligned well with that shown in Fig. 11. The above results proved that the proposed approach possesses favorable stability and reproducibility.

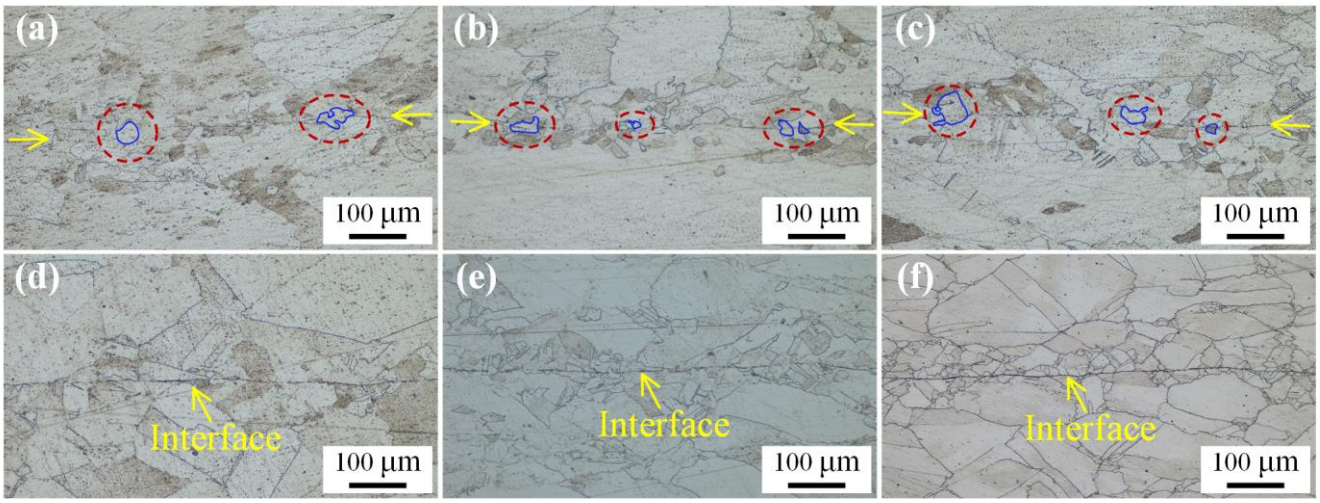

Fig. 12. Cross-section morphologies of repeat experiments. (a), (b), (c) are from different bonding joints treated with the proposed approach. (d), (e), (f) are from different bonding joints without treatment.

Characterizing the microscopic features at the interface is conducive to further understanding of the effectiveness of the proposed approach. Fig. 13 shows the SEM morphologies of the cross-section specimens derived from 1# bonding joint. The vague interface presented in Fig. 10 is composed of several isolated pits with small dimensions. Except for the small pits, most regions achieved a seamless bonding, which can further be seen through Fig. 13 (d), (e) and (f). At the same time, some tiny particles were seen at the bottom of the pits.

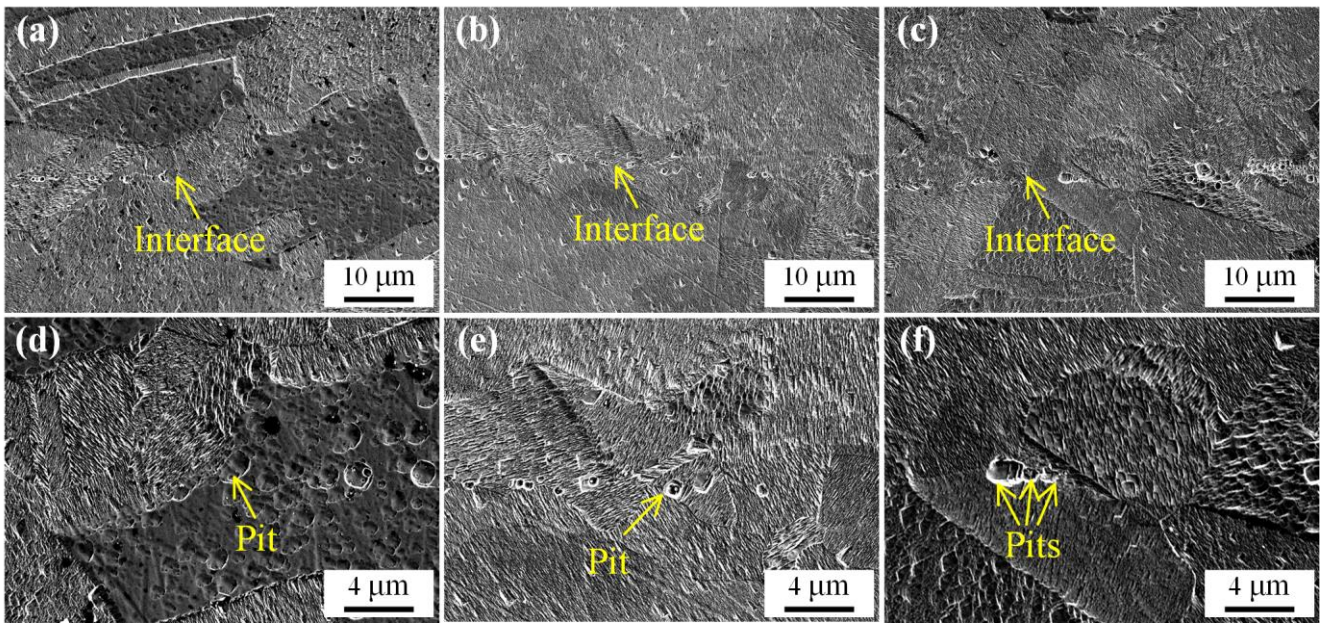

Fig. 13. SEM morphologies of 1# bonding joint. (a), (b), (c) are from different specimens, (d), (e), (f) are the large views of (a), (b), (c), respectively.

The SEM morphologies of various cross-section specimens derived from 2# bonding joint (with native oxide film) are presented in Fig. 14. As shown in Fig. 14 (a), (b) and (c), there are dense pits on the interface. Some particles distributed inside the pits are indicated by the yellow arrows in Fig. 14 (d), (e) and (f). The dimensions of the small particles are about tens to hundreds of nanometers with a spherical shape and the

dimensions of the large particles can reach the micron scale present as an irregularly flat shape.

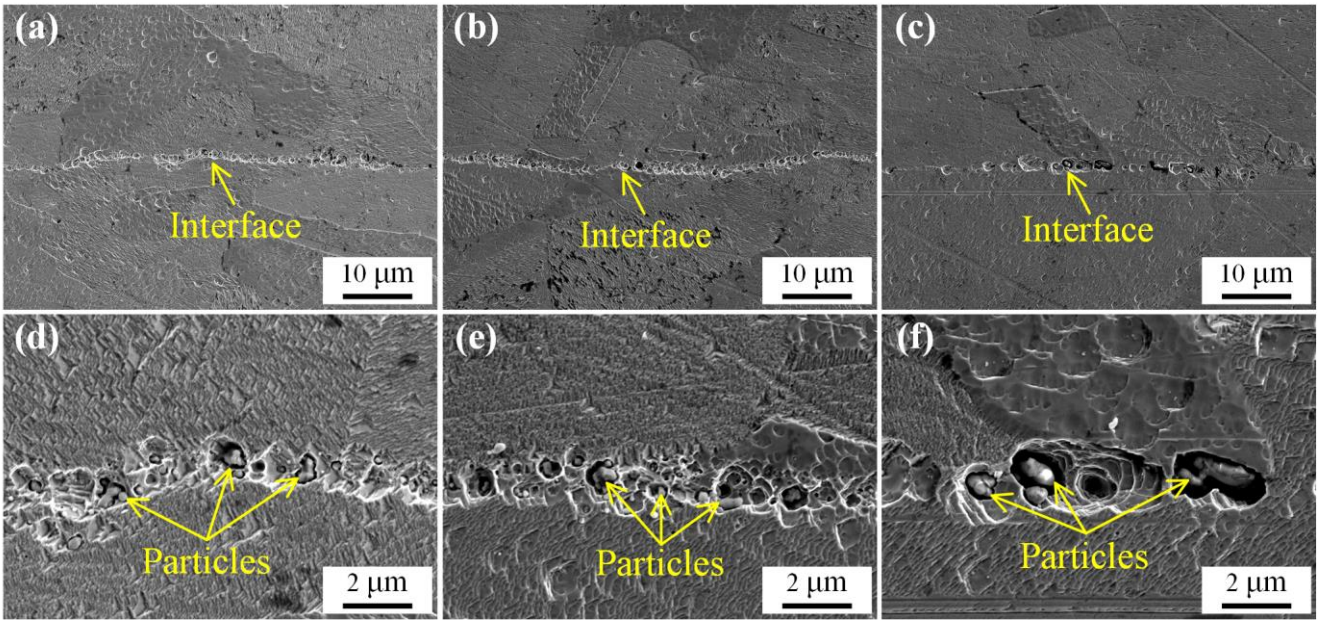

Fig. 14. SEM morphologies of 2# bonding joint. (a), (b), (c) are from different specimens, (d), (e), (f) are the large views of (a), (b), (c), respectively.

Through comparing the cross-section morphologies, it can be found that the interface bonding of the 1# bonding joints is definitely better. The aforementioned results demonstrated the effectiveness of the proposed approach from the perspective of morphology.

4.2.2 Elemental distribution in the interface

The cross-section morphology indicated that the bonding of the 1# bonding joint achieved a nearly seamless bonding which is significantly better than 2# bonding joints. However, some tiny particles were found on the interface. Fig. 15 (a) and (b) show the element of the tiny particles on the interface of the 1# bonding joint. Strong O-peaks were detected, other elements with higher intensities are the matrix elements. The results indicated that the oxygen element had combined with the matrix element and produced the oxide particles. O, Cr and Mn peaks were the main peaks, suggesting that the oxidized particles were oxides of Cr and Mn. A similar result reported that $MnCr_2O_4$ oxide particles existed at the bonding interface of 316 stainless steel after HCB [7]. In addition, a weak Al peak was detected as shown in Fig. 15 (a). Al element may be introduced from the abrasive action of the grinding tool during the pretreatment. The previous study showed that the main element of the abrasive includes Al [35]. In Fig. 15 (b), Fe, Ni, Si and Mo peaks were detected, this can be attributed to the matrix element. EDS point scanning has a detection depth and region; however, the detected particles are small with irregular shape, thus, the results were easily affected by the matrix elements. A small amount of oxide particles was found at the interface of the 1# bonded joint. There are two possible reasons, one is that a vacuum environment was created between interfaces to be bonded, but it is not an absolute vacuum, dilute oxygen may react with the matrix to form small oxide particles.

Another is that a small fraction of the oxide film remains after laser-removing oxide film under vacuum. Either reason is acceptable, it will have almost no impact on the interface bonding quality.

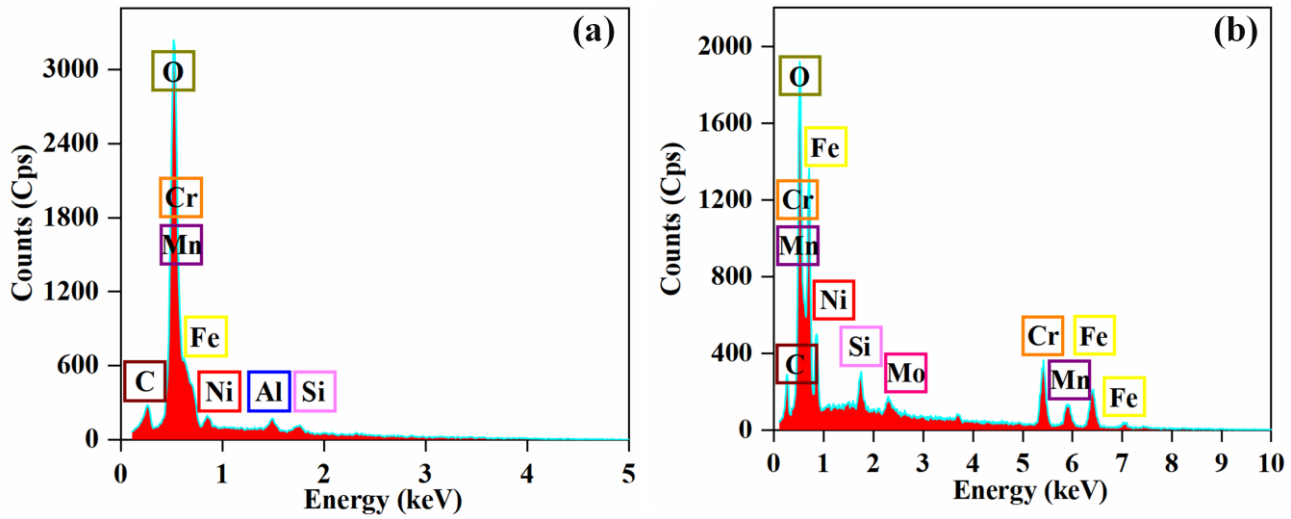

Fig. 15. The element of the tiny particles on the interface of the 1# bonding joint.

Fig. 16 shows the elemental distribution of the cross-section specimen derived from the 2# bonding joint. The results show that the elements of the interface oxides were O, Cr and Mn, which are consistent with the results of interface particles of the 1# bonding joint. However, there is a huge variation of oxide particles in dimension and shape. The oxide particles in Fig. 16 are directly related to the native oxide film on the surface of the original substrate.

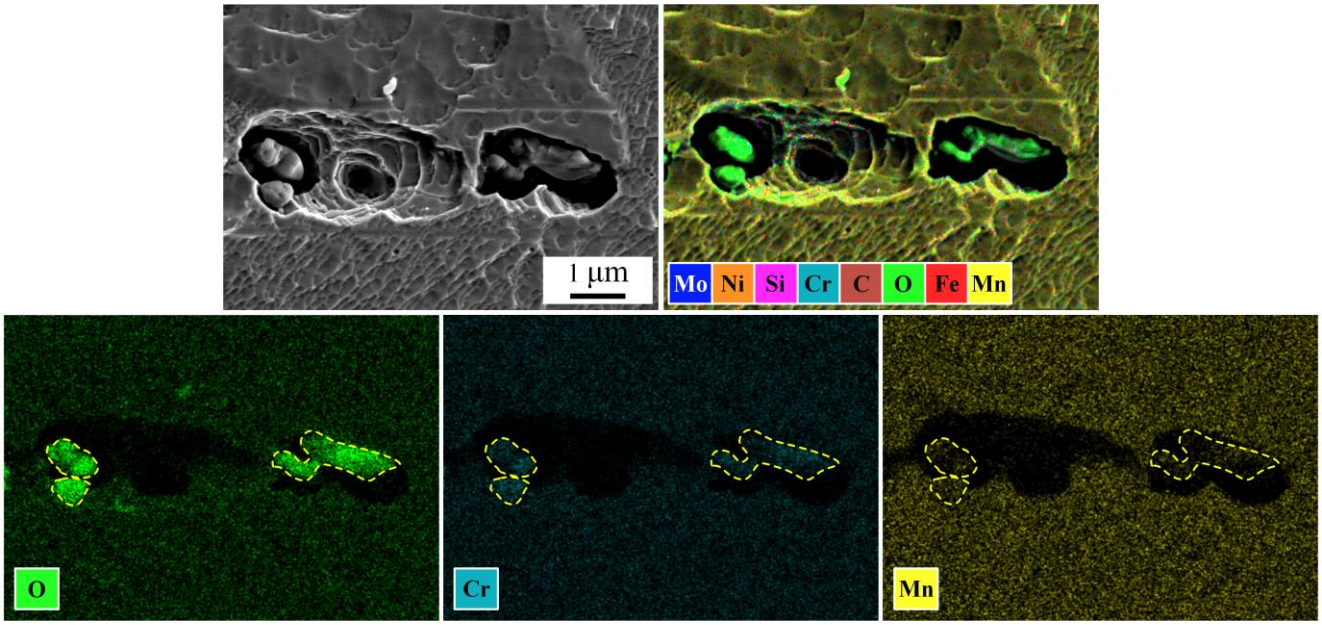

Fig. 16. Element distribution results of cross-section specimen derived from the 2# bonding joint.

To reveal the underlying reason as to why the interfacial residues were O, Cr and Mn oxides, thermodynamic calculations of the interfacial oxides transition for 316H stainless steel under experiment conditions were carried out using Thermo-Calc software with the TCFE10 database. At the beginning of the

HCB, the interfacial oxide film caused an unbalanced state due to high oxygen activity. As the HCB proceeds, the oxygen diffuses into the matrix with low oxygen activity, resulting in a gradual decrease of the oxygen activity at the interface until stabilization. As shown in Fig. 17(a), the residual oxide phase is mainly spinel as the oxygen activity decreases. Fig. 17(b) shows the atomic fraction of elements versus oxygen activity in spinel. The element in spinel mainly contains O, Fe, Cr, Ni and Mn at high oxygen activity. As the oxygen activity decreases, the Fe and Ni show a decreasing trend. Contrarily, the Cr and Mn showed an increasing trend. When the oxygen activity is below 10^{-16}, only O, Cr and Mn are eventually retained. This is consistent with the results shown in Figs. 15 and 16.

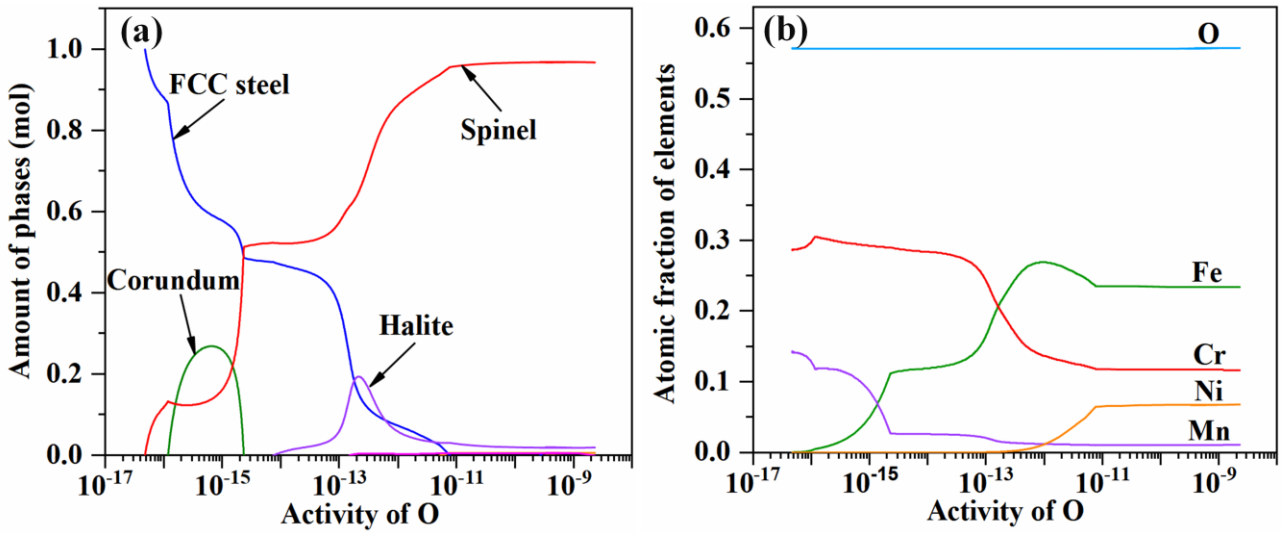

Fig. 17. Results of thermodynamic calculations, (a) number of phases versus oxygen activity, (b) amount fraction of elements in spinel versus oxygen activity.

Elemental characterization together with the thermodynamic calculations proved that the interface particles on the cross-section specimens were oxide particles. The difference of interface oxide particles supported that the proposed approach which used to enhance bonding quality by removing surface oxide film before HCB was effective.

4.2.3 Tensile properties

The tensile properties of the bonded joints produced from the weld sample with native oxide film and oxide film on the surface to be bonded was removed by laser under vacuum were compared. Fig. 18 (a) shows the tensile results of three parallel samples derived from the bonding joints obtained in one comparative experiment. In Fig. 18 (a), I, II and III represent the numbers of three sets of parallel tensile specimens, the red lines are the engineering stress-strain curves of the tensile specimens of the 1# bonding joint and the green lines are that of the 2# bonding joint. As shown in Fig. 18 (a), the UTS and elongation of the 2# bonding joint are much weaker than that of the 1# bonding joint. In addition, there are obvious differences between the stress-strain curves of the 1# and the 2# bonding joints, the tensile specimens of the 2# bonding joint showed a brittle fracture mode. In contrast, the tensile specimens obtained from the 1#

bonding joint exhibits a ductile fracture mode. The uniformity of the three parallel tensile specimens of the 2# bonding joint is poor, which may be due to the uneven distribution of the broken oxide film at the interface. In addition, the interface oxide particles showed different shapes and dimensions, which can variably influence the fracture during the tensile process. There was a group of tensile specimens derived from the 1# bonding joint which differed slightly from the other two groups, which may be due to the uneven recrystallization at the interface. Fig. 18(b) shows the results of repeated experiments on tensile properties, the experiment group adopting the approach, and the control group were subjected to three HCB experiments, respectively. The results of repeated tensile experiments show that the average UTS can reach 430.25 MPa after treatment with the proposed approach. The UTS of the tensile samples was in the range of 414.81 to 449.36 MPa with a standard deviation of 14.88 Mpa; As for the elongation, the average value reached 64.04% with a standard deviation of 7.03%. The tested maximum elongation was 74.00% and the minimum was 56.27%. The relatively narrow standard deviation of UTS and elongation proved that the stability and reproducibility of the proposed approach are favorable. In contrast, for the control group without laser removal of the oxide film under vacuum, the tested average UTS was 371.17 MPa, the UTS of the tensile samples was in the range of 314.58 to 407.03 MPa with a standard deviation of 35.67 Mpa; the average elongation was 26.41% with a standard deviation of 7.13%. The average UTS and elongation of the tensile samples were significantly improved after adopting the proposed approach. In particular, the average elongation was improved exceeding 140%. The above results indicated that the proposed approach has a significant contribution to improving the quality of bonding.

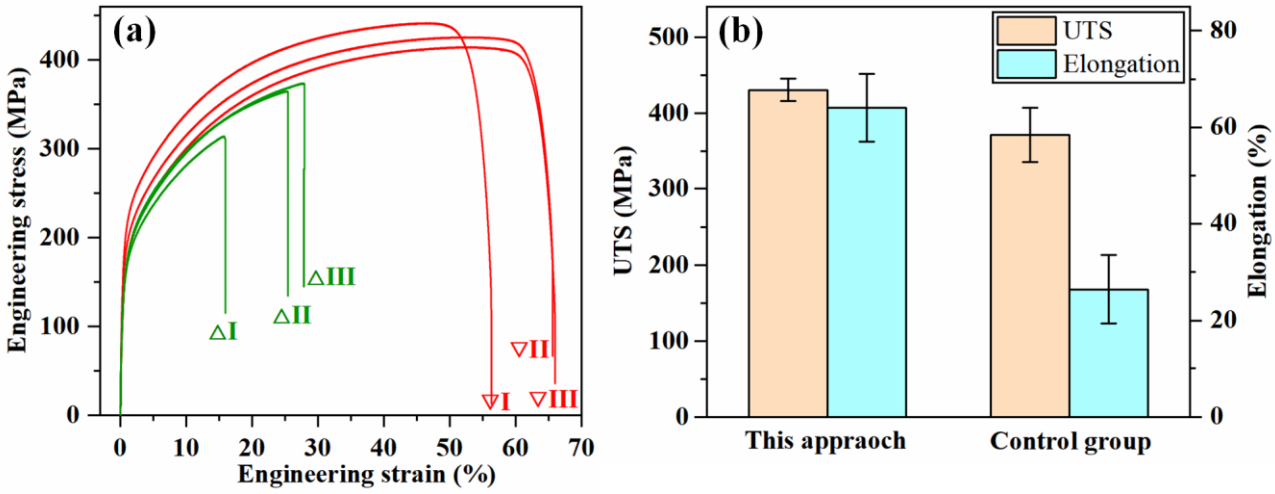

Fig. 18. Results of tensile tests, (a) engineering stress-strain curves, (b) results of repeated experiments.

To gain insight into the reasons for the differences in tensile properties, the fracture morphologies of the tensile specimens were observed. Fig. 19 shows the fracture morphologies of the tensile specimens derived from 1# bonding joints. Fig. 19 I, II and III correspond to the three sets of parallel tensile specimens in Fig. 18 (a). Fig. 19 (a)-(f) are the enlarged view, the enlarged areas were marked by yellow markers. Severe necking occurred in the tensile specimens and the fracture morphologies was seen to consist of two parts,

one is morphology with the large and deep dimples as shown in Fig. 19 (a), (c) and (e), which is distributed in the center of the fracture; another is isometric dimples morphology as shown in Fig. 19 (b), (d) and (f), distributed around the large and deep dimples. The characteristics of the fracture morphology demonstrated the fracture mode of the tensile specimens as ductile fracture, which is consistent with the results of the stress-strain curves. In addition, no oxide particles were found at the bottom of the dimples, indicating that the oxide film was almost thoroughly removed by the laser under vacuum.

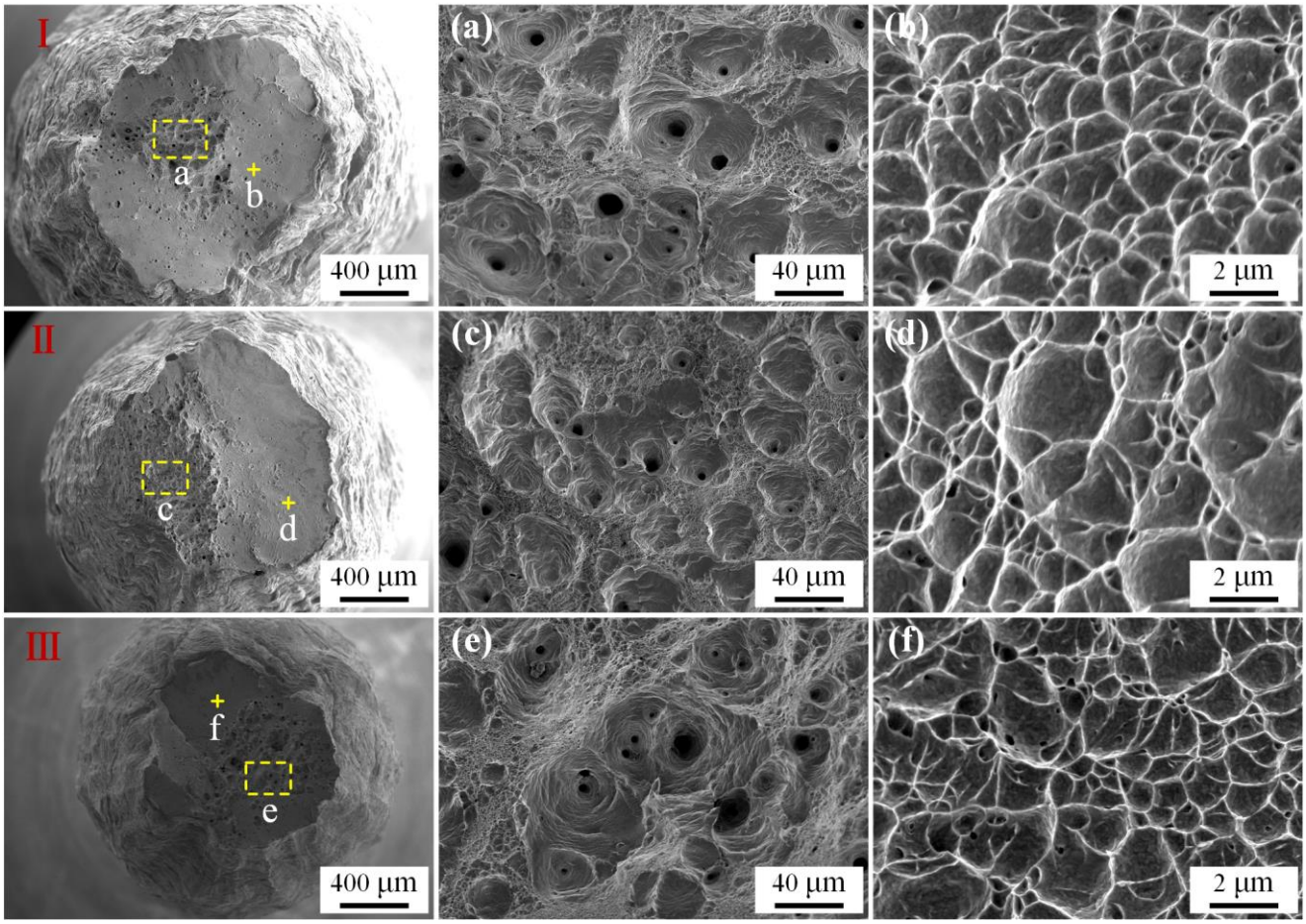

Fig. 19. Fracture morphologies of tensile specimens derived from the 1# bonding joint.

Fig. 20 shows the fracture morphologies of the tensile specimens derived from the 2# bonding joint. The fracture morphologies exhibit a brittle mode of failure which differs from Fig. 19. Fig. 20 I, II and III correspond to the three sets of parallel tensile specimens shown in Fig. 18 (a), Fig. 20(a)-(f) are the enlarged view, the enlarged areas were marked with yellow boxes. As can be seen from Fig. 20 I, II and III, the fracture was flat without involving necking. Grooves produced by grinding during substrate pretreatment were found on the fracture as shown by the yellow dotted lines. The above features confirmed that the interface was not effectively bonded during HCB. Fig. 20 (a), (c) and (e) show a large number of ineffectively bonded regions with shallow and small dimples. Fig. 20 (b), (d) and (f) exhibit the morphologies of the bottom of the dimples and many particles were found as shown by the yellow arrows. The dimensions and shape characteristics of the particles are the same as the particles shown in Fig. 14. The

particles in the dimples act as barriers to prevent interface bonding and as initiation of fracture in the tensile process, leading to fracture of the tensile specimens.

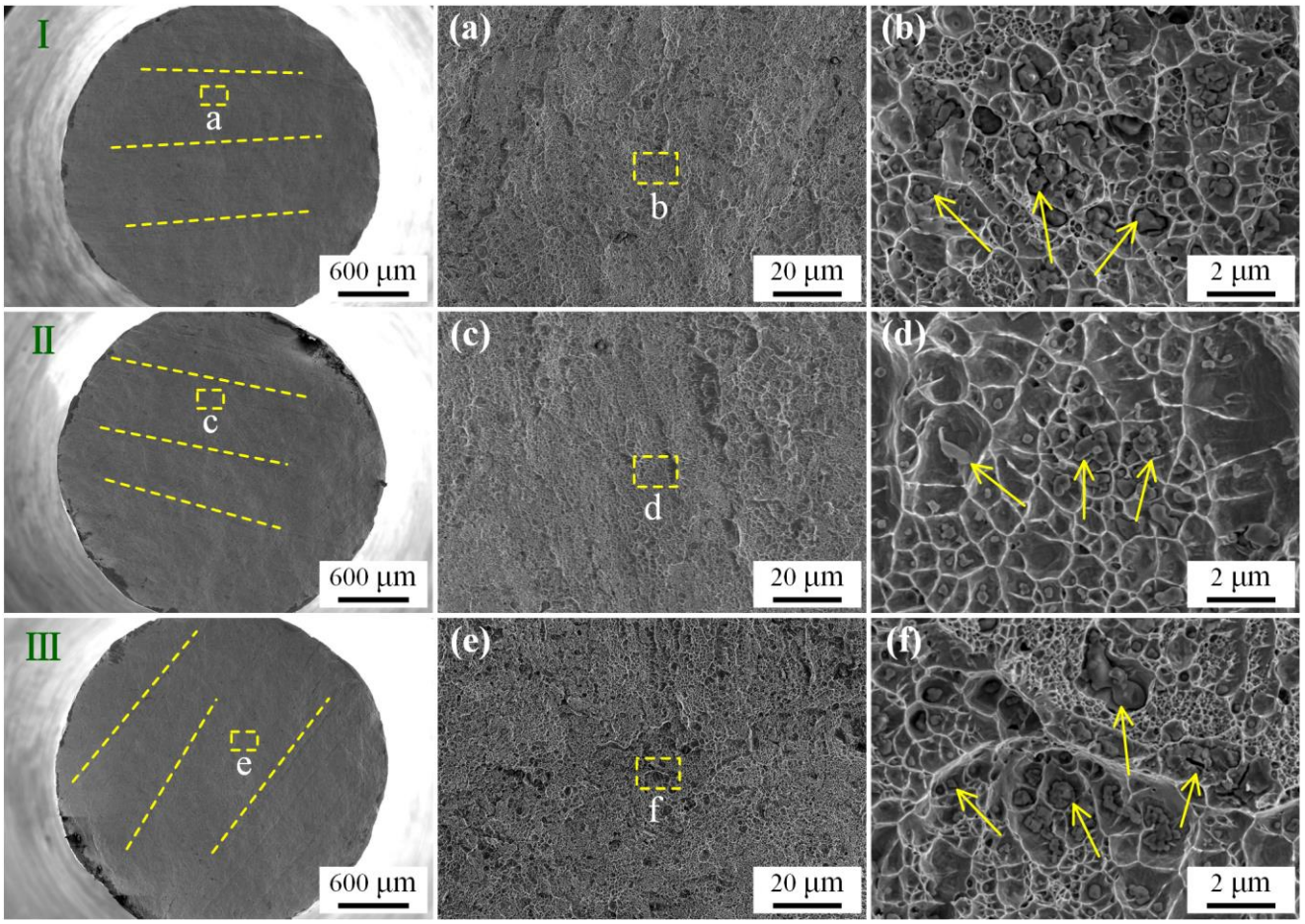

Fig. 20. Fracture morphologies of tensile specimens derived from the 2# bonding joint.

To verify the element of the particles at the bottom of the dimples, the particles in Fig. 20 (b), (d) and (f) were analyzed by point scanning, the results are shown in Fig. 21 (a), (b) and (c), respectively. As shown in the figures, strong O peaks appeared in all the results, which is the main characteristic of the oxide particles generated at the interface of 316 stainless steel during HCB. The results proved that the poor tensile properties of the 2# bonding joint are caused by the obstruction of the oxide particles. The reasons for the peaks of Fe, Ni, Si, Mo and Al are the same as that in Fig. 15.

The results of stress-strain curves and fracture morphologies proved that the interface bonding of the bonding joints compressed by the weld sample with native surface oxide film is seriously hindered, the residual oxide particles at the interface severely impair the tensile properties of the bonding joints. In contrast, the tensile properties of the bonding joints compressed by the weld sample that oxide film on the surface to be bonded was removed by laser under vacuum is better. Oxide particles were not found on the fracture morphologies.

To summarize the interface bonding quality, the 1# bonding joints always outperforms 2# bonding joints in terms of cross-section morphologies, elemental distribution and tensile properties. The above

results confirmed the effectiveness of the proposed approach. In addition, it also proved that the temperature and temperature field simulation results used to screen the laser energy parameters were correct.

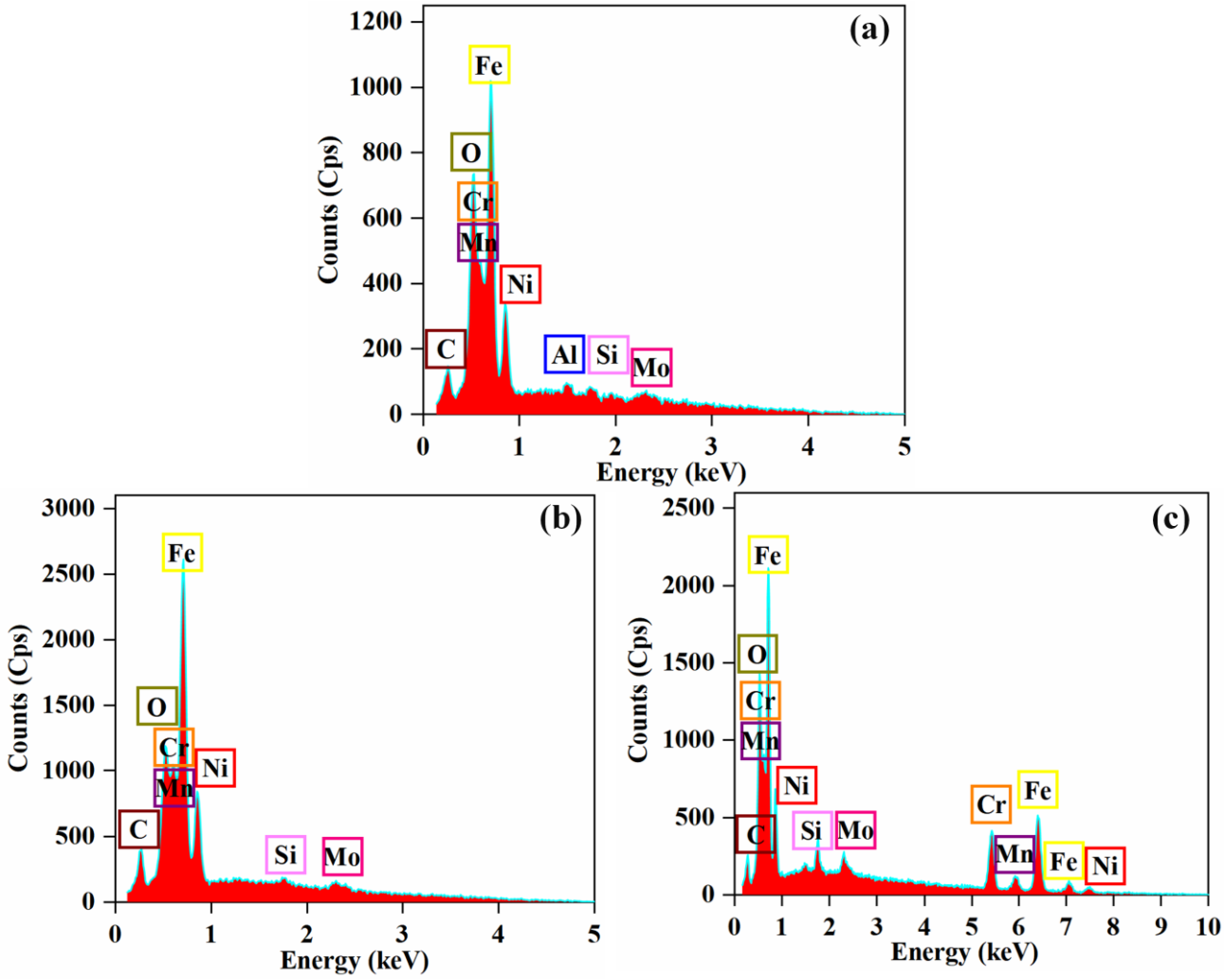

Fig. 21. EDS result of particles on fracture morphologies derived from the 2# bonding joint.

4.3 Suppression mechanisms for interface bonding hindering effect

The suppression mechanisms of the approach were summarized based on the experiment results. As shown in Fig. 22, the substrate surface exists the native oxide film consisting of Fe_2O_3, Fe_3O_4 and Cr_2O_3. When the laser was used to remove the oxide film in a vacuum environment, the heat generated by the laser was higher than the vaporization temperature of the oxide film leading the vaporization of the oxide film. As the laser scans across the area, the fresh metal becomes exposed in vacuum. The vacuum environment isolates external oxygen from the fresh metal surface, preventing secondary oxidation of the fresh surface. It has been reported that the secondary thermal oxidation after laser cleaning can lead to generating a new oxide film on the surface [36], this approach effectively avoids secondary oxidation during laser treatment. The substrates were not immediately removed from the vacuum after removing the oxide film and the surfaces to be bonded were assembled and welded under the same environment. The weld seam shielded the external oxygen and the surface to be bonded continued to remain in vacuum. In this case, the fresh metals

of the surfaces to be bonded were kept in contact and there are barely obstructions between the surfaces to be bonded. During the HCB process, the fresh surfaces to be bonded are in contact tightly without barriers, which is conducive to diffusing. In addition, the recrystallized grains induced by the stress are more easily cross the interface. Ultimately, a nearly seamless bonding was achieved.

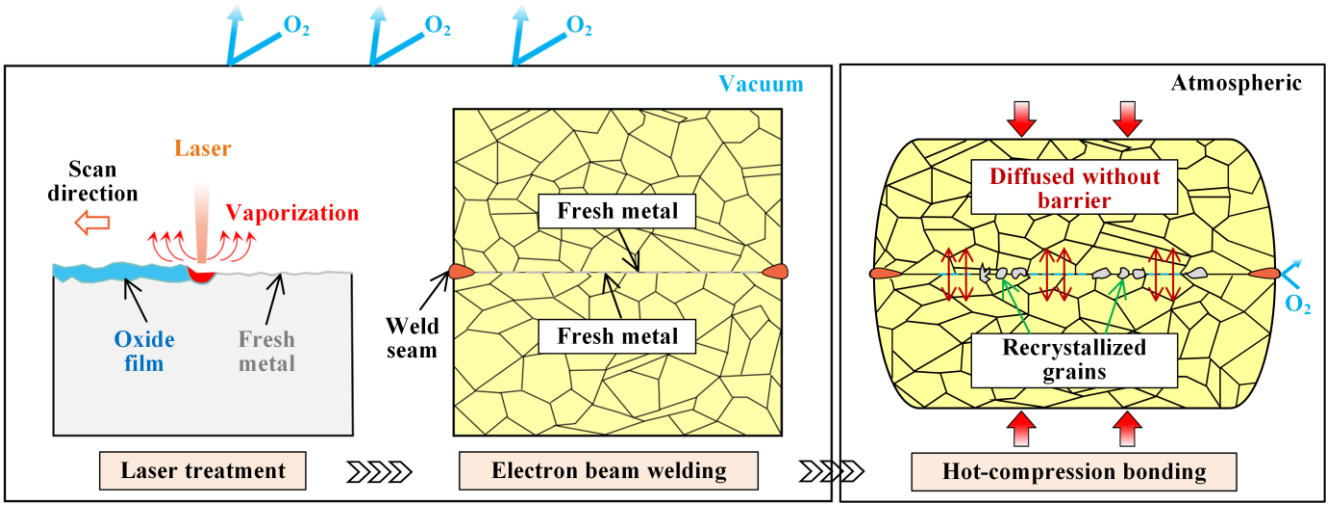

Fig. 22. Suppression mechanisms of bonding hindering effect caused by the oxide film during HCB.

4.4 Advantages and applicability

4.4.1 Technological and Economic advantages

Compared with the existing approaches, the proposed approach in this work possesses some technical advantages, table 3 shows the comparison between the different methods. As for the effectiveness of addressing the oxide film issue to enhance bonding quality, this work is superior to approaches (1) and (3), because the oxide film is removed more thoroughly and secondary oxidation is effectively avoided. It can achieve the same level as approach (2) with a shorter time. Furthermore, the approach proposed in this work can avoid the limitation of approach (2), it has a wider range of applications and is not limited by material type. Since the oxide film was removed, this approach can significantly reduce holding time and lower the deformation and temperature of HCB. Moreover, it removed the oxide film completely without leaving oxygen in the substrate matrix, avoiding the contamination of the substrate material. However, the proposed approach in this work also has limitations, the treatment process is relatively complex than other approaches. The limitation is acceptable because it can produce remarkable effectiveness.

Table 3 the comparison between the different methods

Type of approaches	Effectiveness	Limitations
(1) Breaking the oxide film by external force	The interfacial oxide film is broken, the bonding quality improves	The oxide fragments remains in the interface can still affect the bonding
(2) Diffusing the oxide fragments with high temperatures after breaking the oxide film	Oxygen diffuses into the matrix, the bonding quality can reach a satisfying condition	Only effective for metals that dissolve oxygen; Oxygen remains in the matrix; Rely on high deformation, high temperature and long holding time
(3) Removing surface oxide film under the atmospheric environment before HCB	The number of interfacial oxides decreases; the bonding quality is effectively improved	The fresh metals undergo secondary oxidation; Bonding quality is still impacted by the oxide film
(This work) Removing surface oxide film, assembling and welding the substrate under vacuum before HCB	The surface to be joined is free from the original oxide film and secondary oxidation. The bonding quality was significantly improved	The treatment process is relatively complex

As for economic advantages, to eliminate the effect of the oxide film on bonding quality, the existing approaches need a long holding time with high temperatures to decompose and diffuse the broken interfacial oxide film. Taking 316 stainless steel as an instance, it needs to be held at 1200 ℃ for 18~24 hours [7, 8]. The approach proposed in this work removed the oxide film directly and avoided secondary oxidation at the same time. Therefore, the high-temperature holding with a long time to address the oxide issue can be omitted. This will significantly save the cost of electricity used in the holding treatment process, which is economically advantageous. In addition, when the proposed approach is utilized, the risk of interface bonding failure due to oxide films is greatly reduced, which in turn reduces the economic risk.

4.4.2 Applicability of the approach to other materials

316H stainless steel is an important engineering material for manufacturing large components used in nuclear and solar power plants. This work focused on the engineering requirements for the manufacturing of 316H stainless steel large forgings by additive forging technology, so only 316H stainless steel was discussed. However, this approach is also applicable to other engineering materials that are susceptible to atmospheric oxidation and the oxide film has a severe impact on the bonding quality, such as aluminum alloys and alloy steel. It is worth pointing out that other materials may confront some problems. The parameters of laser removal of oxide film need to match the characteristics of the material to avoid incomplete or over-cleaning. Incomplete cleaning will lead to a residual oxide film and cannot achieve the desired enhancement of bonding quality. Especially for aluminum alloys, the interfacial bonding is more sensitive to the oxide film, the residual oxide film will display a severe impact on the bonding quality. In contrast, over-cleaning can damage the surface of the substrate and cause deterioration of the surface morphology, which is also detrimental to bonding quality. Therefore, the oxide film must be completely removed without damaging the surface of the substrate. The parameters of laser removal of oxide film are

critical, it need to be verified by simulation calculations and HCB experiments.

5. Conclusions

This paper reports a novel approach to remove the surface oxide films from the faying surfaces of stainless steel to obtain seamless joining with improved mechanical strength. The experimentation platform developed to validate the hypothesis has been comprehensively explained and the results obtained from the initial trials are also provided. The proposed new hot-compression bonding (HCB) approach revealed significant improvements. The broad conclusions can be summarized as below:

(1) The proposed approach can significantly enhance the bonding quality. A nearly seamless bonding was achieved after removing the oxide film on the surface to be bonded by laser under vacuum. After using the proposed approach, the average UTS of 316H stainless steel joints improved from 371.17 MPa to 430.25 MPa whereas the average elongation increased from 26.41% to 64.04%.

(2) The suppression mechanisms for interface bonding hindering effect caused by oxide film during HCB was clarified. The oxide film on the surface of the substrate underwent vaporization and the fresh metal was prevented from undergoing any secondary oxidation. This method uniquely enabled us to obtain unobstructed interface bonding. It is conducive to promote the recrystallized grains across the interface, resulting in improved bonding.

(3) The native oxide film formed on the ground surface of 316H stainless steel under atmospheric was characterized and the laser energy for laser-removing oxide film was determined. The native oxide film of 316H stainless steel exposed to air after grinding was composed of metal oxides, metal hydroxides and absorbed water. The metal oxides were mainly Fe_2O_3, Fe_3O_4 and Cr_2O_3. A laser energy of 0.4 mJ was found optimal to ablate the oxide films from the steel surface.

Future work can be directed to use the suggested approach on other classes of engineering materials including aluminum alloys, titanium alloys or dissimilar materials.

Declaration of competing interests

The authors declare that they have no known competing financial interests or personal relationships that could have appeared to influence the work reported in this paper.

Acknowledgments

This work was supported by the National Key Research and Development Program [Grant No. 2018YFA0702900], the Funds for International Cooperation and Exchange of the National Natural Science Foundation of China [Grant No. 52311530080].

References

[1] Sun M Y, Xu B, Xie B J, Li D Z, Li Y Y. Leading manufacture of the large-scale weldless stainless steel forging ring: Innovative approach by the multilayer hot-compression bonding technology. J Mater Sci Technol 2021; 71: 84–86. https://doi.org/10.1016/j.jmst.2020.08.055

[2] Sridharan N, Gussev M, Seibert R, Parish C, Norfolk M, Terrani K, Babu S S. Rationalization of anisotropic mechanical properties of Al-6061 fabricated using ultrasonic additive manufacturing. Acta Mater 2016; 117: 228–237. https://doi.org/10.1016/j.actamat.2016.06.048

[3] Zlatanovic D L, Balos S, Bergmann J P, Rasche S, Zavašnik, J, Panchal V, Sidjanin L, Goel S. In-depth microscopic characterisation of the weld faying interface revealing stress-induced metallurgical transformations during friction stir spot welding. Int J Mach Tool Manu 2021; 164: 103716. https://doi.org/10.1016/j.ijmachtools.2021.103716

[4] Zhao P, Li Z S, Gao X Y, Kuang L L, Xu Z W, Yan J C. A novel diffusion bonding of 6063Al based on a mode of diffusion-migrating and suspension-broken of surface oxide film. J Mater Res Technol 2023; 27: 3719–3728. https://doi.org/10.1016/j.jmrt.2023.10.185

[5] Xu G J, Leng X S, Jing H, Xiu Z Y, Yan J C. Microstructure and strength of ultrasonic-assisted brazed joints of Si_3N_4/ 6061Al composites. J Manuf Process 2020; 54: 89–98. https://doi.org/10.1016/j.jmapro.2020.02.046

[6] Zuruzi A S, Li H, Dong G. Diffusion bonding of aluminium alloy 6061 in air using an interface treatment technique. Mat Sci Eng A 1999; 259:145-148. https://doi.org/10.1016/S0921-5093(98)01004-1

[7] Xie B J, Sun M Y, Xu B, Wang C Y, Li D Z, Li Y Y. Dissolution and evolution of interfacial oxides improving the mechanical properties of solid state bonding joints. Mater Des 2018; 157: 437–446. https://doi.org/10.1016/j.matdes.2018.08.003

[8] Xie B J, Sun M Y, Xu B, Wang C Y, Zhang J Y, Zhao L Z, Li D Z, Li Y Y. Evolution of interfacial characteristics and mechanical properties for 316LN stainless steel joints manufactured by hot-compression bonding. J Mater Process Technol 2020; 283: 116773. https://doi.org/10.1016/j.jmatprotec.2020.116733

[9] Zuo G L, Bai Y, Shi S Y, Tan Z Q, Fan W X, Li Z Q, Hao H. Interfacial healing behavior of CNTs/Al composites in solid-state additive forging. J Manuf Process 2024; 125: 143–154. https://doi.org/10.1016/j.jmapro.2024.07.048

[10] Liu S. RE alloying of GH4169 and additive forging of large-scale disc used in heavy-duty gas turbine. Shenyang: University of Chinese Academy of Sciences, 2022.

[11] Zhu G D, Wang S R, Cheng W, Ren Y, Wen D S. Corrosion and wear performance of aircraft skin after laser cleaning. Opt Laser Technol 2020; 132: 106475. https://doi.org/10.1016/j.optlastec.2020.106475

[12] Shi T Y, Wang C M, Mi G Y, Yan F. A study of microstructure and mechanical properties of aluminum alloy using laser cleaning. J Manuf Process 2019; 42: 60–66. https://doi.org/10.1016/j.jmapro.2019.04.015

[13] Wang W, Li X J, Liu W J, Xing F, Wang J, Zhang K. Experimental study on hydrophobic properties and corrosivity of laser cleaned 7075 aluminum alloy anodized film surface. Opt Laser Technol 2023; 166: 109615. https://doi.org/10.1016/j.optlastec.2023.109615

[14] Li Z C, Xu J, Zhang D H, Xu Z H, Su X, Jin Y, Shan D B, Chen Y B, Guo B. Nanosecond pulsed laser cleaning of titanium alloy oxide films: Modeling and experiments. J Manuf Process 2022; 82: 665–677. https://doi.org/10.1016/j.jmapro.2022.08.033

[15] Dhiman P, Sharma S, Kumar A, Shekh M, Sharma G, Naushad M. Rapid visible and solar photocatalytic Cr(VI) reduction and electrochemical sensing of dopamine using solution combustion synthesized ZnO–Fe_2O_3 nano

heterojunctions: Mechanism Elucidation. Ceram Int 2020; 46: 12255–12268. https://doi.org/10.1016/j.ceramint.2020.01.275

[16] Shi Y H, Wang K, Li H H, Wang H F, Li X Y, Wu X L, Zhang J P, Xie H M, Su Z M, Wang J W, Sun H Z. Fe_3O_4 nanoflakes-RGO composites: A high rate anode material for lithium-ion batteries. Appl Surf Sci 2020; 511: 145465. https://doi.org/10.1016/j.apsusc.2020.145465

[17] Song B Y, Yang M, Liu L H, Zhang X F, Deng Z P, Xu Y M, Huo L H, G S. Biotemplate-derived mesoporous Cr_2O_3 tube bundles for highly sensitive and selective detection of trace acetone at low temperature. Chem Eng J 2022; 450: 138211. https://doi.org/10.1016/j.cej.2022.138211

[18] Perry D L, Tsao L. The galena/dichromate solution interaction and the nature of the resulting chromium(III) species. Inorg Chim Acta 1984; 85 (2): L57–L60. https://doi.org/10.1016/S0020-1693(00)80985-8

[19] Frankcombe T J, Liu Y. Interpretation of oxygen 1s X-ray photoelectron spectroscopy of ZnO. Chem Mater 2023; 35: 5468−5474. https://doi.org/10.1021/acs.chemmater.3c00801

[20] Alshammari T K, Ghoshal S K, Bakhtiar H, Salim A A, Alias S S. Elucidating the structural and spectroscopic attributes of titania-iron oxide (TiO_2-(-Fe_2O_3)) nanocomposites: Showcasing a pulsed laser ablation in liquid approach. Mater Chem Phys 2024; 318: 129235. https://doi.org /10.1016/j.matchemphys.2024.129235

[21] Shi X B, Chu B X, Wang F, Wei X L, Teng L X, Fan M G, Li B, Dong L H, Dong L. Mn-modified CuO, $CuFe_2O_4$, and γ-Fe_2O_3 three-phase strong synergistic coexistence catalyst system for NO reduction by CO with a wider active window. ACS Appl Mater Interfaces 2018; 10: 40509−40522. https://doi.org /10.1021/acsami.8b13220

[22] Cong B W, Hu Y Y, Sun S F, Wang Y, Wang B, Kong H B, Chen G. Metal-organic framework derived amorphous VOx coated Fe_3O_4/C hierarchical nanospindle as anode material for superior lithium-ion batteries. Nanoscale 2020; 12: 16901. https://doi.org /10.1039/c9nr10015f

[23] Moulder J F, Stickle W F, Sobol P E, Bomben K D. Handbook of x-ray photoelectron spectroscopy: A reference book of standard spectra for identification and interpretation of XPS data. Minnesota: Perkin-Elmer Corporation; 1992.

[24] Li W J, Zhou Y N, Fu Z W. Nanocomposite Cr_2O_3–InP as a storage lithium material. J Electrochem Soc 2010; 157(8): A957–A961. https://doi.org/10.1149/1.3446825

[25] Luo H, Dong C F, Xiao K, Li X G. The passive behaviour of ferritic stainless steel containing alloyed tin in acidic media. RSC Adv 2016; 6: 9940–9949. https://doi.org/10.1039/c5ra23698c

[26] Larrañaga M D, Lewis, Sr R J, Lewis R A. Hawley's Condensed Chemical Dictionary. 16th ed. New Jersey: John Wiley & Sons, Inc.; 2016.

[27] Khafidh M, Putera F P, Putera R, Fitriyana D F, Widodo R D, Ismail R, Irawan A P, Cionita T, Siregar J P, Ismail N H. A study on characteristics of brake pad composite materials by varying the composition of epoxy, rice husk, Al_2O_3 and Fe_2O_3. Automot Exp 2023; 6(2): 303-319. https://doi.org/10.31603/ae.9121

[28] Volodin V A, Korchagina T T, Koch J, Chichkov B N. Femtosecond laser induced formation of Si nanocrystals and amorphous Si clusters in silicon-rich nitride films. Physica E 2010; 42: 1820–1823. https://doi:10.1016/j.physe.2009.12.034

[29] Cheng Y Z, Bulgakov A V, Bulgakova N M, Beránek J, Zukerstein M, Milekhin I A, Popov A A, Volodin V A. Ultrafast infrared laser crystallization of amorphous Ge films on glass substrates. Micromachines 2023; 14: 2048. https://doi.org/10.3390/mi14112048

[30] Volodin V A, Cheng Y Z, Bulgakov A V, Levy Y, Beránek J, Nagisetty S S, Zukerstein M, Popov A A, Bulgakova N M. Single-shot selective femtosecond and picosecond infrared laser crystallization of an amorphous Ge/Si multilayer stack. Opt Laser Technol 2023; 161: 109161. https://doi.org/10.1016/j.optlastec.2023.109161

[31] Papynov E K, Portnyagin A S, Modin E B, Mayorov V Y, Shichalin O O, Golikov A P, Pechnikov V S, Gridasova E A, Tananaev I G, Avramenko V A. A complex approach to assessing porous structure of structured ceramics obtained by SPS technique. Mater Charact 2018; 145: 294–302. https://doi.org/10.1016/j.matchar.2018.08.044

[32] Li Z C, Zhang D H, Su X, Yang S R, Xu J, Ma R, Shan D B, Guo B. Removal mechanism of surface cleaning on TA15 titanium alloy using nanosecond pulsed laser. Opt Laser Technol 2021; 139: 106998. https://doi.org/10.1016/j.optlastec.2021.106998

[33] Guo H, Martukanitz R, Debroy T. Laser assisted cleaning of oxide films on SUS409 stainless steel, J Laser Appl 2004; 16: 236–244. https://doi.org/10.2351/1.1809639

[34] Liu H H, Miyagaki T, Lim Y, Kamai M, Fujii H. A novel pressure-controlled joule-heat forge welding method to fabricate sound carbon steel joints below the A_1 point. J Manuf Process 2021; 68:770–777. https://doi.org/10.1016/j.jmapro.2021.06.008

[35] Zhao Y, Xie B J, Zhang, J L, Wang, Q Q, Xu B, Guo J, Jin Z J, Kang R K, Li D Z. Effects of surface roughness on interface bonding performance for 316H stainless steel in hot-compression bonding. Acta Metall Sin-Engl 2023; 36: 771–788. https://doi.org/10.1007/s40195-023-01533-8

[36] Liu B W, Wang C M, Mi G Y. Simulation of the removal mechanism of thermo-oxidized layer and surface morphological evolution on TA15 alloy under nanosecond pulsed laser ablation by multiphase flow model. J Manuf Process 2021; 69: 69–83. https://doi.org/10.1016/j.jmapro.2021.07.038